Recent degradation of Interior Alaska permafrost mapped with ground surveys, geophysics, deep drilling, and repeat airborne LiDAR

Thomas A. Douglas[1,*], Christopher A. Hiemstra[1], John E. Anderson[2], Robyn A. Barbato[3], Kevin L. Bjella[1], Elias J. Deeb[3], Arthur B. Gelvin[1], Patricia E. Nelsen[1], Stephen D. Newman[3], Stephanie P. Saari[1], Anna M. Wagner[1]

[1]U.S. Army Cold Regions Research and Engineering Laboratory, 9th Avenue, Building 4070, Fort Wainwright, Alaska, USA 99709
[2]U.S. Army Geospatial Research Laboratory, Richmond, Virginia, USA
[3]U.S. Army Cold Regions Research and Engineering Laboratory, 72 Lyme Road, Hanover, NH, USA 03755

Correspondence to: Thomas A. Douglas (Thomas.A.Douglas@usace.army.mil)

Abstract. Permafrost underlies one quarter of the northern hemisphere but is at increasing risk of thaw from climate warming. Recent studies across the Arctic have identified areas of rapid permafrost degradation from both top-down and lateral thaw. Of particular concern is thawing syngenetic "yedoma" permafrost which is ice rich and has a high carbon content. This type of permafrost is common in the region around Fairbanks, Alaska and in a region of Central Alaska that expands westward to the Seward Peninsula. A major knowledge gap is relating belowground measurements of seasonal thaw, permafrost characteristics, and talik development with aboveground ecotype properties and thermokarst expansion that can readily quantify vegetation cover and track surface elevation changes over time. This study was conducted from 2013-2020 along four 400 to 500 m long transects near Fairbanks, Alaska. Repeat end-of-season active layer depths, near-surface permafrost temperature measurements, electrical resistivity tomography (ERT), deep (>5 m) boreholes, and repeat airborne Light Distance and Ranging (LiDAR) were used to measure top-down thaw and map thermokarst development at the sites. Our study confirms previous work using ERT to map surface thawed zones, however, our deep boreholes confirm the boundaries between frozen and thawed zones that are needed to model top down, lateral, and bottom-up thaw. At disturbed sites seasonal thaw increased up to 25% between mid-August and early October and suggests active layer depth measurements must be made as late in the fall season as possible because the projected increase in the summer season of just a few weeks could lead to significant additional thaw. At our sites, tussock tundra and spruce forest are associated with the lowest mean annual near-surface permafrost temperatures while mixed forest ecotypes are the warmest and exhibit the highest degree of recent temperature warming and thaw degradation. Thermokarst features and perennially thawed zones (taliks) have been identified at all sites. Our measurements,

when combined with longer-term records from yedoma across the 500,000 km^2 area of central Alaska show widespread near-surface permafrost thaw since 2010. Projecting our thaw depth increases, by ecotype, across the yedoma domain we calculate 0.44 Gt of permafrost soil ~~C have been~~ thawed over the past 7 years, an amount equal to the yearly CO_2 emissions of Australia. Since the yedoma permafrost and the variety of ecotypes at our sites represent much of the Arctic and subarctic land cover, this study shows remote sensing measurements, top-down and bottom-up thermal modelling, and ground based surveys can be used predictively to identify areas of highest risk for permafrost thaw from projected future climate warming.

1 Introduction

Permafrost underlies ~40% of central Alaska, a 500,000 km^2 region stretching east to west from the Canadian border to the Seward Peninsula and north to south from the Brooks Range to the Alaska Range. This is expected to mostly disappear from the near surface (upper 1 m) by 2100 (Pastick et al., 2015). Mean annual air temperatures in interior Alaska, currently roughly -2°C (Jorgenson et al., 2020), are projected to increase by 2°C by 2050 (Douglas et al., 2014) and 5 °C by 2100 (Lader et al., 2017). Roughly half of the discontinuous permafrost in the area represents late Pleistocene ice and organic carbon rich "yedoma" (Kanevskiy et al., 2011; Strauss et al., 2016). In total, yedoma contains almost a third of the permafrost carbon pool despite underlying only 625,000 km^2 of central Alaska and Russia, ~7% of the total global permafrost land area (Heslop et al., 2019). Yedoma permafrost contains large organic carbon stocks that are extremely biolabile (Vonk et al., 2013; Strauss et al., 2017; Heslop et al., 2019) and highly vulnerable to thaw due to high ice content and the prevalence of massive ice bodies, particularly ice wedges (Strauss et al., 2013; 2017).

Throughout much of central Alaska the permafrost is undergoing widespread top down and lateral thaw (Jorgensen et al., 2013; 2020; Douglas et al., 2020; Circumpolar Active Layer Monitoring Network, 2020). Recent measurements of lateral thaw (Neumann et al., 2019) and modelled bottom up thaw (McClymont et al., 2013; Way et al., 2018) of discontinuous permafrost bodies have also been reported. Permafrost degradation alters hydrogeology, soils, vegetation, and microbial communities (Racine and Walters, 1994; Walker et al., 2006; Mackelprang et al., 2011; 2017; Wilhelm et al., 2011; Wolken et al., 2011; Messan et al., 2020). Microbiological and trace metal processes are also likely to change in thawing permafrost ecosystems due to alterations in soil, vegetation, and wetland properties (Grosse et al., 2011; Douglas et al., 2013; Schuster et al., 2018; Burkert et al., 2019). In addition to these ecological and hydrologic changes, permafrost degradation presents an expensive and uncertain challenge for the design, siting, and maintenance of vertical and horizontal infrastructure in cold regions (Hjort et al. 2018).

The thermal state of near surface permafrost is controlled by topography, slope, aspect, soil texture, ground ice content, air temperature, hydrology, land cover, snow depth and timing, and liquid precipitation (Osterkamp and Romanovsky, 1999; Jorgenson and Osterkamp, 2005; Myers-Smith et al., 2008; Loranty et al., 2018). In relatively warm areas like Interior Alaska, the permafrost is "ecosystem protected" (Shur and Jorgenson, 2007) by an insulating organic-rich soil, plant litter, and vegetation surface layer. Disturbance to this insulating layer from

climate warming, infrastructure development, or wildfire increases ground heat flux and promotes top down, lateral, and bottom-up thaw (Viereck et al., 1973; Yoshikawa et al., 2003; Nossov et al., 2013).

Commonly, the first signal of an altered permafrost thermal state is an increased seasonally-thawed "active" layer (Hinkel et al., 2003; Shiklomonov et al., 2010). Seasonal trends in active layer depth, particularly across a variety of ecotypes, can provide information on how and where permafrost degradation features initiate and expand. Low-ice content dry sandy soils typically have deeper active layers than ice rich silt or organic-rich soils (Brown et al., 2015; Loranty et al., 2018). As such, active layer measurements can infer information about subsurface soil characteristics. When top-down permafrost degradation occurs, the active layer depth may increase before any readily identifiable change in surface vegetation or geomorphology occurs. The most pronounced terrain surface features form when thaw of ice rich permafrost leads to thermokarst (hollows formed by ground subsidence following thaw of ice-rich permafrost; Kokelj and Jorgenson, 2013; Brown et al., 2015; Douglas et al., 2016). Thermokarst features include lakes, bogs, fens, and pits in lowlands and thaw slumps and active-layer detachments in uplands (Smith et al., 2005; Jorgenson et al., 2013).

There is a need to broadly apply remotely-sensed analyses to identify high ice content permafrost at risk of top down and lateral thaw degradation to support ecological, hydrologic, and engineering, investigations. Identifying risk factors for thermokarst initiation typically requires combining ground-based surveys and remotely-sensed measurements. Where permafrost is associated with surface biophysical characteristics that can be measured remotely, standoff detection tools like airborne LiDAR and repeat imagery analysis can be applied toward tracking trajectories of change over large regions (Jones et al., 2013; Chasmer and Hopkinson, 2016; Lewkowicz and Way, 2019). Geophysical techniques, predominantly electrical resistivity tomography (ERT), have been recently coupled with airborne and active layer measurements to detect thermokarst development and associate ice content with terrain geomorphology (Yoshikawa et al., 2006; Douglas et al., 2008; Lewkowicz et al., 2011; Hubbard et al., 2013; Minsley et al., 2015; Bjella, 2020) and biophysical characteristics (Douglas et al., 2016) at broader scales. A combination of repeat active layer measurements, geophysical surveys, and airborne LiDAR have been used to map subsurface permafrost bodies, quantify top-down thaw, and identify locations where thermokarst features have been initiated or expanded (Douglas et al., 2016; Rey et al., 2020). Long-term ground-based time series measurements can be combined with ERT to quantify top down thaw, track the initiation and lateral expansion of thermokarst features, and identify where ecosystem characteristics influence the permafrost thermal regime. Further, extents of the base and sides of discontinuous permafrost bodies with geophysical measurements confirmed with deep boreholes is needed to monitor and better model lateral and bottom-up thaw.

The objective of this study was to establish relationships between ecotype, permafrost soil characteristics, and seasonal thaw across a variety of terrains in interior Alaska. Our sites represent 159,000 km^2 of high ice content yedoma permafrost with massive ice wedges that is present across the 500,000 km^2 expanse of central Alaska (Strauss et al., 2016). We made repeat seasonal and active layer thaw depth measurements, performed electrical resistivity tomography, and characterized the permafrost with boreholes up to 15 m deep along transects that represent the five most common ecotypes associated with central Alaska's yedoma permafrost. Ground-based information was combined with high-resolution repeat airborne LiDAR imagery to identify thermokarst initiation and quantify terrain elevation changes over time. Long term active layer depth measurements across central Alaska were used to place our measurements into spatially broader and temporally longer scales. We used our active layer-ecotype relationships to model the amount of yedoma permafrost carbon that has thawed across central Alaska since 2013. The goals of this work were to measure seasonal thaw and thermokarst development over time and identify surface and subsurface terrain properties that can be remotely quantified, like vegetation type and thaw subsidence, with permafrost geophysical, soil, and active layer characteristics.

2. Study Area

~~2.1 Study location and Site Descriptions~~

Our field sites are located near Fairbanks, Alaska (Fig. 1). The region has a continental climate with a mean annual air temperature of -2.4ºC, typical mean summer temperatures of 20°C, mean winter temperatures of -20°C, and yearly extremes ranging from 38°C to -51°C (Jorgenson et al., 2001; 2020). Mean annual precipitation is 28.0 cm (Wendler and Shulski, 2009) with a typical annual snowfall of 1.7 m (Jorgenson et al., 2001) that represents 40-45% of the annual precipitation (Liston and Hiemstra, 2011). Discontinuous permafrost features in the area are up to 60 meters thick and are located primarily in lowlands, along north-facing slopes, and where soils or vegetation provide adequate thermal protection (Racine and Walters, 1994; Jorgenson et al., 2008; Douglas et al., 2014). Permafrost at our field sites is Pleistocene syngenetic ice-rich "yedoma" formed through repeated deposition of windblown loess and organic matter (Shur and Jorgenson, 2007; Douglas et al., 2011; Strauss et al., 2016). Almost a third (181,000 km^2) of the global yedoma permafrost is in Alaska and of that the majority is in a swath of central Alaska between the Brooks Range to the north and the Alaska Range to the south (Strauss et al., 2016). Carbon content in the permafrost of 2–5% (~10 kg/m^3) is up to 30 times greater than unfrozen mineral soil (Strauss et al., 2013).

Our field investigations were organized along four transects crossing a variety of lowland (n=3) and upland (n=1) permafrost landscapes (Fig. 1). The 400 m "Farmer's Loop 1" and 500 m "Farmer's Loop 2" transects were located at 64.877°N, 147.674°W and 64.874°N, 147.677°W, respectively. These two transects cross a variety of ecotypes including mixed deciduous forest (dominated by *Picea glauca* and *Betula neoalaskana*), *Salix spp.* riparian wetland, *Eriophorum vaginatum* tussock tundra, and moss- black spruce (*Picea mariana*) forest. Trail crossings and other clearings (disturbed areas), devoid of trees, punctuate the transects in multiple locations and are inhabited by the grass *Calamagrostis canadensis*. A nearby Circumpolar Active Layer Monitoring (CALM) site has a 16-year active layer record (CALM, 2020). A 500 m transect at the nearby Creamer's Field Migratory Waterfowl Refuge (64.868°N, 147.738°W) transitions from mixed deciduous forest (*Betula neoalaskana* and *P. glauca*) in the first 150 m, before entering moss- black spruce (*P. mariana*) forest for ~50 m. Farther north on this transect *Eriophorum vaginatum* tussock tundra is prevalent with isolated *B. neoalaskana* and *P. mariana* trees along with two east-west oriented trail crossings. A 400 m southwest-northeast oriented transect was also established above the CRREL Permafrost Tunnel in Fox, Alaska (64.950°N, 147.621°W). Vegetation at this site transitions from black spruce (*P. mariana*) forest with S*phagnum* moss through 1960s-era clearings and trails and shrub-dominated (*Rhododendron groenlandicum* and *Betula nana)* clearings into Glenn Creek's riparian zone. Our field sites encompass common boreal ecoregion land cover classes (sub-polar needleleaf and deciduous forest, mixed forest, shrubland, grassland; wetland, barren; disturbed; and water). Together, these classes account for 74% of the boreal ecoregion's area in North America (Latifovic et al., 2017).

3. Material and Methods

3.1 Satellite and LiDAR imagery

Imagery was needed to examine transect land cover types corresponding with LiDAR data. Cloud-free high-resolution Maxar WorldView-2 (WV 2) satellite imagery (2 m multispectral; 0.5 m panchromatic) was obtained for all sites (Fig. 1) on 7 June 2020. The images were orthorectified and pan-sharpened using ENVI's 5.5.3 SPEAR pan-sharpening (Gram-Schmidt) to qualitatively maximize the imagery to match LiDAR data. Airborne LiDAR measurements ~~are~~ helpful for monitoring surface changes and examining surface roughness characteristics. LiDAR data ~~collected in 2010 were only available for the~~ Creamers Field Transect ~~(Hubbard et al., 2011). These data were collected by aircraft 5-6 May 2010~~ using an Optech ALTM Gemini ~~(Toronto, Canada)~~ 1064 nm LiDAR with a pulse frequency of 70 ~~k~~Hz and 12° scan angle~~. The~~ resulting point cloud (point density = 4 points/m^2) was

used to create a 1.21-m resolution digital surface model (DSM) with a vertical ~~accuracy~~ of 16 cm. ~~All three of the sites (Fig. 1) were scanned with a different LiDAR platform 17-18 May 2020. An aircraft-mounted Leica (Wetzlar, Germany) ALS80 (1064 nm) acquired surface returns at an average density of ≥25 points/m^2. In both the 2010 and 2020 collections, aircraft and sensor position and attitude data were indexed by GPS time for post-processing correction and calibration. Measurement accuracy yielded a root mean square error (RMS) of ≤6.6 vertical cm in 2020.~~ Point clouds ~~were~~ processed to create hydro-flattened ~~raster surfaces~~ with a spatial resolution of 0.25 m. Hydro-flattening ~~was used to~~ remove errant point cloud elevation artefacts from resulting ~~digital elevation models (DEMs)~~ given water's low reflectance. In this process, stream, pond, and lake boundaries ~~were~~ identified and the DEM ~~was~~ corrected to more accurately portray water level elevation given the identified shoreline, yielding a waterbody-smoothed product. Changes in elevation at the Creamer's Field site between 2010 and 2020 were calculated by subtracting 2010 elevations from 2020 elevations (2020 minus 2010) using raster algebra to delineate elevation losses (negative values) and gains (positive values) over the 10 year period.

3.2 Field survey measurements, coring, and meteorology

In May-June 2013, 1-m wide trails were delicately hand cleared of large woody vegetation along linear transects to improve access for repeat surveying and geophysical measurements. A Trimble (Sunnyvale, California USA) R8 DGPS was used to survey pin flag measurement markers at a 4 m spacing along each of the four transects. We used a 1 cm diameter 1.7 m long graduated metal rod ("frost probe") to make seasonal thaw depth measurements at each flag location to quantify the end of summer season "active" layer (Shiklomonov et al., 2013). Measurements were repeated in mid-October from 2013 to 2020, however, in 2014 additional measurements were made in June, July, and August. Active layer measurements from 2013 to 2017 were published previously (Douglas et al., 2020).

A Geoprobe 7822 Direct Push Technology track mounted drill rig was used to collect ~~deeper (between 4 and 15.6 m deep)~~ cores in late winter and spring 2014. Coring was limited to locations that had trail access for the heavy tracked vehicle. Three wood fragments found in cores from the Farmer's Loop transects were analysed for ^{14}C age and $\delta^{13}C$ measurements following commonly used radiocarbon analytical procedures at Beta Analytic (Miami, Florida). A SIPRE corer was used to collect 2 to 3 m deep cores in the spring of 2017 and 2018 at locations representing the major ecotypes at each site following established methods (Douglas et al. 2011). Gravimetric (Geoprobe) or volumetric (SIPRE) moisture contents were measured following established methods (Phillips et al., 2015).

An Onset (Bourne, Massachusetts, USA) HOBO U23 Pro v2 external temperature and relative humidity logger with a solar radiation shield was installed 2 m above the ground surface at the Permafrost Tunnel and Farmer's Loop sites. Onset HOBO U23 Pro v2 two channel external temperature loggers were installed at depths of 1.2 m at nine locations across our field sites at locations where this represents permafrost. The thermistor was protected by a plastic sleeve and installed into the ground after a 0.75 cm diameter hole was excavated using a slide hammer and rod.

3.3 Electrical resistivity tomography

We used a "SuperSting" R8 eight channel portable induced polarization galvanic earth resistivity meter ~~(Advanced Geosciences Incorporated, Austin, Texas)~~ for ERT ~~measurements~~. ERT measurements were conducted in mid-summer 2013 using six cables, each with 14 take-out electrodes. Our electrode spacings of 2.5 to 4 m achieved a maximum subsurface penetration depth of ~30 m. We used a dipole-dipole array because it represents spatial aspects of ice-rich terrain and provides horizontal resolution sufficient for detecting vertical structures in permafrost (Kneisel, 2006; Douglas et al., 2016). Contact resistance was measured at each electrode prior to initiating the survey to ensure cable connectivity. At rare instances when contact resistances were higher than 2,000 Ω-m salt water ~~was added~~ around the electrode and contact resistance was re-measured until resistance fell below 2,000 Ω-m. Electrodes were typically 45 cm long but electrodes up to 3 m in length were used in areas with thick vegetation mats or moss.

We used RES2DINV (Geotomo Software, Penang, Malaysia) to perform two-dimensional model interpretation. The software provides signal smoothing and constrains inversion with finite difference forward modeling and quasi-Newton techniques (Loke and Barker, 1996; Loke et al., 2003). A least-squares inversion achieves convergence by comparing changes in ~~root mean squared (~~RMS~~)~~ quadratic error between two and five iterations, then three and five iterations, etc. Convergence was achieved when RMS error values reached ~10% convergence and further iterations would not significantly lower the RMS values.

4. Results

4.1 Satellite and LiDAR imagery

The four transects we studied contain five dominant ecotypes of the boreal biome and central Alaska yedoma terrain (mixed deciduous forest, wetlands, tussock tundra, moss- black spruce forest with a thick moss cover, and

disturbed; Douglas et al., 2020). The Creamer's ~~f~~ield transect starts in birch forest, transitions to mixed forest, and at 140 m it transitions abruptly to tussock tundra for the remainder of its 500 m length (Figs. 2a and 3a). Patterned ground (near-surface ice wedge polygons) is readily evident in the airborne LiDAR in the mixed forest along the first ~150 m of the transect (Fig. 2b). This area is characterized by high-centered polygons up to 2 m ~~high~~ that form when ice wedges melt. When the transect transitions to tussock tundra, ice wedge polygons are no longer as strongly visible at the ground surface, yet, polygonal ground is evident in true color satellite imagery and airborne LiDAR throughout the remainder of the transect (Figs. 2a and 3a). Winter trails, dominated by native graminoids, are evident in the true color and LiDAR images at 290 m and 460 m.

There is subtle evidence of ice wedge polygons along the two transects at the Farmer's Loop field site (based on WV 2 satellite images and LiDAR; Figs. 4a, 4b, 5a, and 5b). Both transects start in mixed forest that extends for ~120 m. Transect 1 crosses a small wetland feature at 80 m before transitioning to tussock tundra until 310 m. After a graminoid-dominated trail the ecotype changes to *P. mariana* (black spruce) forest. Farmer's Loop transect 2 shifts from mixed forest (*B. neoalaskana*, *Salix* spp., and *P. glauca*) to a flow through fen wetland from 120 to 170 m. After a trail crossing at 200 m the ecotype shifts abruptly to tussock tundra until the 400 m mark where a trail crossing separates the tussock tundra from mature *P. mariana* (black spruce) forest.

Though ice wedges are present throughout the 300 m of subsurface passages that run partially below the Permafrost Tunnel transect they are covered by a ~5 m thick surface layer of Holocene silt (Hamilton et al., 1988) and a thick veneer of mosses, lichen, shrubs, and trees. Polygonal ground is not identifiable in visible (WV 2) or LiDAR imagery at the surface along the Permafrost Tunnel transect (Figs. 6a and 6b). The Permafrost Tunnel Transect originates in spruce forest, transits through shrubland, and crosses trails and Glenn Creek before entering black spruce forest again. Numerous trail crossings identified as disturbed locations and a large thermokarst feature near Glenn Creek ~~are~~ also present. Anthropogenic features (i.e. disturbances) like roads, trails, and clearings~~,~~ are easily identifiable in the satellite imagery at all sites.

Our longest LiDAR data series spans May 2010 to 2020 and is limited to the Creamers Field transect (Fig. 7). ~~A~~ difference in ~~those elevations (2010 elevations were subtracted from 2020 elevations)~~ indicates substantial elevation losses (over 1 m of subsidence) along the northern edge of degrading polygon ice wedges in an area that has transformed into an elongate lake. This thaw front of degrading permafrost is evident along the southern margin of the transect (left side of the map). Water levels in the pond and in some ice wedge polygon troughs

show higher elevations in 2020 compared to 2010 (0.2 to 1.0 m) due to ~~deeper and more persistent~~ precipitation ~~in the last three years.~~

4.2 Field survey measurements, coring, and meteorology

The mid-June and early August seasonal thaw depth measurements and October active-layer measurements in 2014 show a steady downward movement of the thaw front throughout the summer season (Figs. 2c, 3c, 4c, 5c, and 6c). The majority (~80%) of the summer season thaw at the tussock tundra and spruce forest sites occurs by early August. However, in the wetland, disturbed, and mixed forest ecotypes the increase in thaw depth from early August to mid-October is up to one third of the eventual active-layer depth. This is particularly evident along the first 200 m of the Farmer's Loop 2 transect (Fig. 5c). The wetland, disturbed, and mixed forest ecotypes yield the deepest active layers at all sites. The tussock tundra and spruce with moss ecotypes consistently yield the lowest seasonal thaw measurements and show little change between August and October. A statistical summary of the active-layer depths is provided in Table 1. It is clear that for all five ecotypes active-layer depths increased substantially between 2013 and 2020. Since each ecotype is associated with different starting thaw depths the percent increase in depth between 2013 and 2020 is a good indicator of top down thaw over the seven year period. The tussock, wetland, disturbed, and mixed forest ecotypes all exhibited increases in active-layer depth of more than 50 percent while the increase in the spruce forest was 33 percent. Across all five ecotypes the mean of active layer depth in 2013 was statistically significantly smaller than the measurement in 2020.

We collected 14 deep (greater than 5 m) cores with the Geoprobe and 12 shallow (3 m or less) SIPRE cores (Figs. 2d, 3d, 4d, 5d, and 6d). Frozen bulk density (SIPRE cores; frozen mass divided by volume) and gravimetric moisture content (Geoprobe cores; mass of water lost through drying divided by volume) from the cores are included in Table S1. In general, the upper-most core samples, which consisted of surface vegetation and organic matter, yielded the greatest moisture content values. Most of the cores had peat or organic and ice-rich permafrost in the upper 1-3 meters and along some deeper sections and these typically yielded gravimetric moisture contents greater than 100%. The deeper permafrost soils were characterized as ice rich ~~and~~ ice poor silts and sands with gravimetric moisture contents of 60-150% which is similar to measurements of syngenetic yedoma type permafrost in the Permafrost Tunnel (Bray et al., 2006; Douglas et al., 2011; Douglas and Mellon, 2019). For the subset of SIPRE cores that yielded frozen bulk density values ~~they~~ ranged predominantly between 900 and 1400 kg~~/m^3~~ which is also similar to values from the nearby Permafrost Tunnel, however, some ice rich and peaty zones yielded values above 1400 kg~~/m^3~~.

Coring allowed us to confirm that large decreases in apparent resistivity values from ERT confirmed 0°C isotherm boundaries between frozen and thawed material. Notably, a deep core ~~on~~ the Farmer's Loop 1 transect ~~(at 358 m)~~ ~~collected~~ thawed silt from 9.15-10.35 m. The ERT measurements at that location show a large thawed region starting at ~10 m depth identified by resistivity values of ~1,000 Ω-m (more discussion below). Along the ~~sides~~ of most of the thawed zones we identified ~~at each site~~ marked changes in apparent resistivity allowed identification of the lateral boundaries of thermokarst features. Notably, these include thawed zones in the high-centered polygons along the beginning of the Creamer's Field transect, thermokarst pits along the Farmer's Loop and Permafrost Tunnel transects, a large (~50 m) lateral expansion of the thermokarst toward the end of the Permafrost Tunnel transect, and thawed regions below numerous disturbed areas at all sites. Some of the 2017 and 2018 SIPRE cores identified ~~seasonal taliks~~ between the bottom of the winter frozen layer and the top of the permafrost (Table S1). For example, a 2017 core from the mixed forest at 87 m along Farmer's Loop ~~transect~~ 1 yielded thawed silt from to 46 to 102 cm. Cores collected in 2018 along Farmer's Loop ~~transect~~ 2 in mixed forest at 71 m ~~collected~~ thawed silt from 84-117 cm and two cores from the Permafrost Tunnel ~~(~~at 52 and 305 m~~)~~ ~~identified~~ thawed silt from 31-49 cm and 45-70 cm, respectively. These thawed zones are located above the typical ~~active layer depth~~ for those locations and indicate the ~~winter freeze did not extend downward to the top of the permafrost~~.

4.3 Radiocarbon dating

We obtained ^{14}C ages from wood fragments collected from three Geoprobe core samples through Geochron Laboratories (Chelmsford, Massachusetts, USA). An age of 10,360 ~~+/-~~ 360 calibrated years before present (cal. YBP) ($\delta^{13}C$: -27.7 ‰) was measured at a depth of 1.02 m in the tussock area at 306 m on Farmer's Loop ~~transect~~ 1 (Supplementary Table 1). At 358 m along the same transect and also in the tussock area at 0.67 m depth the ^{14}C age was 10,160 ~~+/-~~ 160 cal. YBP ($\delta^{13}C$: -28.0 ‰). Along the Farmer's Loop 2 transect, in the spruce forest at 420 m and at a depth of 0.49 m depth a wood fragment yielded a ^{14}C age of 7,200 ~~+/-~~ 190 cal. YBP ($\delta^{13}C$: -28.7 ‰).

4.4 Air and ground temperature measurements

Air temperature, wet (rain) and dry (snow) precipitation, and the snowpack depth, from April 1, 2013 through October 31, 2014, are provided in Fig. 8. This time period encompasses when the repeat summertime thaw depths and geophysical analyses were measured. The meteorological measurements were made by the National Weather Service at the Fairbanks International Airport (PAFA) 8 km to the southwest of the Creamer's Field and Farmer's

Loop transects and 17 km southwest of the Permafrost Tunnel transect. Air temperatures at the Permafrost Tunnel and Farmer's Loop sites are also included and they did not deviate substantially from one another or from the 90 year PAFA mean during the timeframe of the study. Air temperatures ~~went~~ above 0°C around the middle of May and did not go below freezing again until late October. The summer of 2013, when our ERT measurements were made, experienced a total of 14.5 cm of ~~wet precipitation~~ which is slightly lower than the 90 year mean of 18.5 cm. The 2013 summer mean temperature of 12.2 °C was close to the 90 year summer mean of 11.8 °C. (Jorgenson et al., 2020). In terms of heating degree days the summer of 2013 (1133) was slightly above the historical mean of 1090. The winter of 2013-2014 total snowfall of 1.22 m was slightly below the historical mean of 1.7 m. The wet precipitation total for the summer of 2014 (37.1 cm) was anomalously higher than the mean.

Fig. 9 provides mean annual ground temperatures (MAGT) at 1.2 m depth for ~~our field sites~~ represent~~ing~~ the range of ecotypes at our sites. ~~When they were installed~~ in 2013 this depth represented the upper 40-60 cm of permafrost ~~at our sites~~. We also provide the mean annual ground temperature at 1.2 m depth for each site between October 1, 2013 and October 1, 2019 (Table 2). The Creamer's Field disturbed site, in a clearing devoid of permafrost 114 m southeast of the Creamer's Field transect, is the only location where the mean annual soil temperature at 1.2 m is above freezing (4.31 °C). The remaining thermistors emplaced to 1.2 m depth are located in permafrost and their temperatures remained below 0 °C for the entire record, however, they all show warming between 2013 and 2019. Thermistors in the mixed forest and spruce forest ecotypes have been steadily approaching 0 °C. Mean annual permafrost temperatures at the two mixed forest sites (-0.24 and -0.20 °C) and spruce forest (-0.25 °C) are substantially higher than for the three tussock tundra thermistor locations (-1.55, -1.39, and -2.60 °C). The tussock tundra sites also have the lowest winter permafrost temperatures.

4.5 Electrical resistivity tomography

Electrical resistivity tomography measurements across the transects (Figs. 2e, 3e, 4e, 5e, and 6e) provide insight into the presence or absence of permafrost at depths of up to 40 m~~eters~~ below the ground surface, particularly when they are calibrated with subsurface information from boreholes. Resistivity values of ~800 Ω-m and higher have been reported for syngenetic permafrost near Fairbanks while values below 800 Ω-m are generally assumed to represent thawed material (Hoekstra and McNeill, 1973; Harada et al., 2000; Yoshikawa et al., 2006; Douglas et al., 2008; 2016; Minsley et al., 2016). For the Creamer's Field transect (Figs. 2 and 3) the first 130 m consists of actively degrading ice wedge polygons that are present along a slightly-elevated bench (~3 m) in mixed forest. In this area, pockets of low resistivity material in the upper 1-2 m denote the thawed areas around the high-centered

polygons. Permafrost (1.2 m depth) temperatures at this location have increased steadily since 2013 and are currently are only slightly below freezing (Fig. 9). This is the same region that exhibits the largest rates of ground subsidence in repeat LiDAR differencing at the site (Fig. 7). The greatest active-layer depths along the Creamer's Field transect are located in this area. It is noteworthy that at some locations ~~in~~ this ~~area~~ of the transect the ~~active layer expanded~~ ~25% between late August and early October. Clearly the permafrost along the first ~75 m of the transect is undergoing active thaw degradation. At 140 m along the transect the ground surface ~~drops slightly~~ and from there to the end of the transect the ecotype is characterized as tussock tundra. The permafrost in the tussock region is colder (MAGT at 1.2 m: -1.55°C) with little ~~downward expansion of the active layer~~ between late August and early October. The lone exception is a small (2-5 m across) thermokarst feature at a transect distance of 380 m that exhibits anomalous thaw throughout the summer and is barely discernible in the aerial image, LiDAR, and ERT measurements.

Both of the Farmer's Loop transects (Figs. 4 and 5) start in a mixed forest for the first ~125 m. In this area the near surface permafrost is comprised of silts with minor peat and some layers with low gravimetric moisture contents of ~23-50 ~~g/g~~. These areas also have the deepest active layer depths. Some small thawed areas as well as disturbed areas and small wetland features are identifiable by resistivity values of 200-700 Ω-m in the upper few meters and active layers more than a meter deep. As with the Creamer's Field site these ecotypes are associated with the largest increase in active-layer depth between late August and early October. Permafrost in this area appears to be present for only the upper 15 to 20 m. A small flow through fen from 120 to 180 m along Farmer's Loop transect 2 has a low resistivity region ~15 m below the ground surface. These areas are associated with the warmest permafrost temperatures at the Farmer's Loop site (-0.05 °C at 1.2 m; Fig. 9; Table 2).

Once the transect transitions into tussock tundra the active-layer depths become shallower and the temperatures at 1.2 m decrease. Regions of anomalously low ERT measurements are associated with small surface thermokarst features, water features, or disturbed areas. Soils in the area are characterized as silts with varied ice contents. A deep drill hole at 358 m along Farmer's Loop ~~transect~~ 1 identified thawed material starting at 915 ~~cm~~ and this corresponds with the marked decrease in resistivity values at this same location and depth.

At the permafrost tunnel site (Fig. 6) the ERT resistivity values are 1,000 to 2,000 Ω-m in the upper ~4 m with a repeating pattern of markedly higher values (5,000 to 10,000 Ω-m) from 4 to 10 m in depth and at a ~10 m spacing. This is consistent with ice wedge polygon structures in the subsurface, likely the "Upper Silt Unit" overlain by Holocene silts as mapped by Hamilton et al. (1988) and corroborated by our core drilling at the site. These

subsurface ice wedge structures do not extend to the surface and, as such, they do not relate to vegetation type, or seasonal thaw depths changes across the transect. Towards the far end of the Permafrost Tunnel transect the ERT from 2014 identifies the lateral edges of a large thermokarst feature forming at the site. Thaw between 2014 and 2020 has added roughly 25 m of width to both sides of the feature.

5. Discussion

The results from this study clearly show, through a variety of corroborating measurements, ice-rich yedoma permafrost in the area around Fairbanks, Alaska has been warming and actively degrading in numerous locations. Four major lines of evidence show permafrost thaw degradation has been initiated and is likely increasing at our sites. First, active layer measurements show thaw depths have been increasing across all ecotypes since 2013 (Table 1), however, some ecotypes experience deeper seasonal thaw than others. In 2014, the only year when we made repeat thaw depth measurements during the summer, (Figs. 2-6 c and d) it is apparent that in mid-June there is minimal variability in thaw depth except for some of the disturbed areas that eventually exhibit the deepest active layer thickness. By mid-July the disturbed and mixed forest ecotypes exhibit the most seasonal thaw and these ecotypes have the deepest end of season active-layer depth measurements. In some locations, particularly the disturbed sites, mid-August seasonal thaw depths and early October active layer measurements show a ~20% increase over that 6 week period. The length of the summer growing season in the area has increased by 38 days (Wendler and Shulski, 2009) and our thermistor measurements (Figure 9) show peak soil temperatures at 1.2 m typically occur in late November. From this, it is clear that the timing of thaw depth measurements may have to be pushed later into the fall to adequately represent the summer season, particularly in mixed forest and wetland ecotypes (Figures 2-6). This has ramifications for field studies where thaw depth measurements are made in August during the end of most field seasons. ~~Increasingly, these measurements will not represent the true active layer depth.~~

Previous studies have established that vegetation provides a range of ecosystem protection properties for permafrost (Shur and Jorgenson, 2007; Loranty et al., 2018). Recent measurements confirm this and identify strong links between different ecotypes and top-down thaw of permafrost in Interior Alaska (Yi et al., 2018; Douglas et al., 2020; Jorgenson et al., 2020; Kropp et al., 2020). In this study, some ecotypes are associated with consistently deeper active layer measurements over time. Disturbances, like trail crossings, are associated with dramatically deeper seasonal thaw than any other ecotypes and some of them are also expanding laterally. Removal or alteration of the organic soil layer or moss ground cover increases the ground heat flux and promotes

more rapid seasonal and permafrost thaw (Nicholas and Hinkel, 1996) due to the loss of the "ecosystem protection" of permafrost in the area (Shur and Jorgenson, 2007). In many locations at our field sites, active layer depths have increased since 2013 to greater than 2 m which is greater than typical winter freezeback. Infrastructure development and wildfire are the most likely ways for land cover to change to a disturbed ecotype. Post-fire forest succession to a mixed forest, which is increasingly occurring across Interior Alaska and much of the boreal biome, will also undoubtedly lead to warmer surface soils and more top-down permafrost thaw (Kasischke and Johnstone, 2005; Johnstone et al., 2010; Jafarov et al., 2013; Brown et al., 2015). Tussock tundra and some of the spruce forest sites yield the shallowest active layer depths. As such, if vegetation were to change from tussocks or spruce to a mixed forest or disturbed (i.e. no moss or forest vegetation) land cover the potential risk of top-down permafrost thaw would increase considerably.

Our results support recent work at our study sites that show the disturbed, mixed forest, and wetland ecotypes exhibit the deepest active layers (Douglas et al., 2020). That study presents measurements from 2014 to 2017 at the same sites presented here and links deeper active layer depths with wetter summers. The four additional years presented here show the thaw front has continued to migrate downward despite the lack of anomalously wet summers in 2018 and 2019. At most sites the 2020 active layer depths are the deepest in the record and the comparatively shallower thaw depths measured in 2013 have not been repeated at any site since then.

The increase in active layer depths we measured at our sites since 2013 is similar to the longer-term trend represented at all six Circumpolar Active Layer Monitoring sites spread across 500,000 km^2 of central Alaska (the east-west swath south of the Brooks Range and North of the Alaska Range; Figure 10; CALM, 2020). At most sites a steady increase in active layer depth was initiated around 2010 and has continued since. Within this region of central Alaska 159,000 km^2 of the permafrost has been identified as yedoma. This represents roughly 25 percent of the total global yedoma permafrost area of 625,000 km^2 (Strauss et al., 2016). Using the regions mapped as yedoma ~~as a "cookie cut" clipping~~ from ecotype maps that cover all of central Alaska (Jorgenson and Meidlinger, 2015; Raynolds et al., 2019) we calculate the five ecotypes in our study represent 90% of the total land cover on top of yedoma permafrost. Mixed forest (34%), moss-spruce forest (23%), wetland (20%), and tussock tundra (13%) are widely prevalent while disturbed sites are not identified, likely due to their small spatial scale. Using the 2013-2020 increase in active layer from our field measurements, projecting the area of each ecotype across the central Alaska domain mapped as yedoma, and using the mean organic carbon concentration in yedoma permafrost of 10 ~~kg/m^3~~ from Strauss et al. (2013) we calculate the total central Alaska yedoma permafrost organic

carbon (OC) pool that has thawed since 2013 as 0.44 Gt OC. This does not include non-yedoma permafrost in the same region that likely has also thawed since 2013.

Additional evidence indicating thaw of near-surface permafrost at our sites includes some thermistor measurements showing at 1.2 m depth approaching and eventually warming above 0°C (Fig. 8) at some sites. Mixed forest sites have warmed the most and all three of our 1.2 m deep thermistors in this ecotype exhibit a steady warming that has been retarded at ~-0.1°C, likely due to latent heat effects in the transient layer and below (Boike et al., 1998; Shur et al., 2005). The tussock and spruce forest ecotypes do not show the steady increases in permafrost temperatures, however, the overall trend in mean annual temperatures at 1.2 m depth at these sites is increasing (Table 2).

The third indication of near-surface permafrost ~~degradation~~ is the widespread development of ~~supra-permafrost taliks (an unfrozen layer between the active layer and the top of the near-surface permafrost) zones developing)~~ at our sites indicated by SIPRE cores collected in 2017 and 2018. At many locations, the seasonal thaw has proven to be deeper than the depth of winter freeze-back. The ~~seasonal taliks~~ we found are located predominantly in the mixed forest and disturbed ecotypes. These areas contain the warmest near-surface permafrost and in some cases the low ice content sandy silts have a higher thermal conductivity that promotes the movement of heat into the ground. At some of these sites we ~~have~~ had to augment ~~thermistors at 1.2 m depth by~~ installing deeper (i.e. 2 to 2.5 m ~~thermistors~~) to maintain measurements of the near-surface permafrost ~~temperatures when the thaw front reaches 1.2 m~~. Since thaw depths increased in 2019 and 2020 it is likely these ~~taliks have expanded vertically and laterally.~~

Numerous lines of visual evidence provide the fourth indication of active permafrost thaw in our research area. The most dramatic is that of the ground subsidence associated with permafrost thaw in the mixed forest region of the Creamer's Field transect (Fig. 9). Ice wedge polygons in the area have warmed steadily since 2013 and repeat LiDAR analysis shows ~~development of~~ high-centered polygons development has expanded due to melting ice wedges (Fig. 7). This suggests potential hydrologic and soil thermal process changes are ongoing in that area (Liljedahl et al., 2016). Anomalous thaw depths coinciding with recent development of thermokarst pits are evident in airborne LiDAR and true color images at all of our sites. At the Creamer's Field site degradation of ice wedge polygons is evident in our repeat LiDAR analysis. ~~The~~ most ~~dramatic~~ thaw subsidence occurred in the mixed forest area ~~represented by~~ the first 150 m of ~~our~~ transect. ~~In this area~~ near-surface permafrost soils, comprised of lower ice content silts and sands, are warmer and high-centered polyons ~~were already forming when~~

we initiated our study. Some of the low-lying troughs between polygons, particularly those along the thaw front next to the ponded area to the west, have ~~dropped~~ by 1-1.5 m in the decade from 2010 to 2020. ~~Further out this transect in some select areas~~ it appears ground elevations of the polygon troughs increased between 2010 and 2020. ~~We~~ attribute this to ~~this~~ area being extremely low lying and more standing water ~~being present~~ in the troughs from snowmelt in May 2020 compared to 2010. Due to ~~the~~ standing water we ~~cannot~~ ascertain whether the ice wedges in this area ~~have~~ melted ~~at all~~.

Repeat yearly active-layer depth measurements show that the thermokarst features have been ~~extending~~ vertically downward and horizontally since 2013. Examples are at the Creamer's Field transect at ~100 m; Farmer's Loop ~~transect~~ 1 at 68 m and 360 m; Farmer's Loop ~~transect~~ 2 at 8 m, 88 m, 116 m, and 408 m; and the Permafrost Tunnel transect at 64 m, 108 m, 140 m, and particularly at 328 m. These thermokarst features are forming either in areas of mixed forest with low ice content and a higher sand content or in locations where ice wedges are present and are likely melting. The mixed forest ecotypes have the warmest mean annual temperatures and are thus at risk of thaw due to warming temperatures while the areas with ice wedges can exhibit dramatic subsidence as the ice melts.

Our study further confirms recent studies showing ERT measurements provide a robust way to characterize frozen versus thawed zones in permafrost terrains (Lewkowicz et al., 2011; Hubbard et al., 2013; Minsley et al; 2016; Douglas et al., 2008; 2016; Rey et al., 2020; Bjella, 2014; 2015; 2020). High resistivity areas identify permafrost while low resistivity values correspond with thawed zones at the surface. Hotspots of low resistivity values correspond with deep active layer measurements, for example, at disturbed sites and across thermokarst features where thaw is identifiable from airborne imagery and LiDAR. Few studies have coupled ERT measurements with deep boreholes to corroborate the bottom or lateral extent of permafrost yet mapping these 0°C isotherm boundaries is critical for tracking and modelling lateral and top-down thaw. At the 358 m distance on the Farmer's Loop 1 transect our borehole encountered a thawed zone at ~10 m that corresponds exactly with the bottom of frozen soil measured by the large decrease in resistivity at that location (Fig. 4). Our ERT results show discontinuous permafrost is present at depths of up to at least 25 m across all transects but the lateral extent of small surface and subsurface thawed regions (as of 2014) are identifiable in ERT measurements at all sites.

The deep boreholes, in some cases representing the bottom of permafrost where bottom-up thaw is occurring (McClymont et al., 2013) also provided access to wooden fragment samples amenable for ^{14}C dating. ~~This allowed us to relate age and depth at three site locations.~~ Based on the relationship between core depth and age date at the

three ~~locations~~ where we have ^{14}C ages we calculate syngenetic permafrost ~~deposition~~ rates of 0.7 to 1 mm per year. This is close to the rates measured in the Permafrost Tunnel (Hamilton et al., 1988;) and these ~~deposition~~ rates are important for mapping and modelling permafrost lateral and vertical extent across remote locations.

6. Conclusions

The variety of measurements used in this study all confirm that near-surface permafrost around Fairbanks, Alaska has been undergoing ~~dramatic~~ warming and widespread thermokarst development since our measurements started in 2013. The majority of the warming and thaw degradation are occurring in mixed forest ecotypes with low ice content sandy-silt soils, however, remote sensing evidence shows thermokarst features have been initiated in all of the ecotypes represented. ~~Though~~ tussock tundra and spruce forest ecotypes ~~are associated with~~ the lowest mean annual near surface permafrost temperatures at 1.2 m depth ~~our results show warming below these ecotypes as well. Thermistors at 1.2 m depth at the tussock and spruce forest sites reach the coldest winter temperatures of all our sites so~~ winter processes may ~~be~~ control~~ling~~ the potential future thermal state of permafrost below these ecotypes. Based on CALM site measurements, mapping, and geospatial analyses we conclude the rapid and extensive thaw we identified at our field sites ~~are~~ common across the 500,000 km^2 area of central Alaska. Since the yedoma-type permafrost at our field sites and across the larger region is ice rich and has a high carbon content there is high risk of thaw degradation and impacts to the carbon cycle. Based on our calculations the total central Alaska yedoma permafrost organic carbon (OC) pool that has thawed since 2013 ~~as~~ 0.44 Gt OC. For perspective, this is slightly more than the yearly CO_2 emissions of Australia (Friedlingstein et al., 2019). Results from this study can support large scale modelling efforts on how current and projected future land cover will armour permafrost against thaw and disturbance ~~but~~ also how and where ecotype changes can increase the risk of permafrost thaw and thermokarst development. Our study sites are well suited to support these types of analyses because the area contains warm permafrost, the climate has been warming since the 1970s, and our transects represent most of the land cover present in the boreal and taiga of the Arctic and subarctic. The relationships we found between ecotype, permafrost composition, and seasonal thaw dynamics can be used to apply biophysical characteristics and standoff measurements like repeat aerial imagery, hyperspectral measurements, and LiDAR, to ascertain the presence or absence of permafrost in similar terrains. This will help ~~apply~~ three-dimensional thermal models ~~to~~ top-down, lateral, and bottom-up that of discontinuous permafrost bodies so future climate projections can better be applied toward identifying the likely response of permafrost to warming.

Data availability Repeat seasonal thaw depth measurements (2014), repeat active layer measurements (2014-2020), and yedoma area carbon content calculations are available through Zenodo using doi: 10.5281/zenodo.4670463. All project geophysical data are available through reasonable request.

Author contribution

TAD, CAH, and JEA designed and initiated the study and performed field work; RAB, KLB, EJD, ABG, SDN, SPS, and AMW assisted in the field and analysed data; PEN oversaw geospatial and mapping analyses; all authors contributed to development and writing of this manuscript.

Competing Interests

The authors declare no competing interests.

Acknowledgements

This research was funded by the U.S. Army Corps of Engineers Engineer Research and Development Center Basic Research Program under PE 0601102/AB2 (Protection, Maneuver, Geospatial, Natural Sciences) and Center Directed Research Program and the Department of Defense's Strategic Environmental Research and Development Program (Projects RC-2110 and RC18-1170). We thank Amanda Barker, Sam Beal, Marc Beede, Maria Berkeland, Dana Brown, Seth Campbell, Jarrod Edwards, Tiffany Gatesman, Malcom Major, Margaret Rudolph, Torre Jorgenson, Merritt Turetsky, Simone Whitecloud, and Caiyun Zhang for help with field measurements. We appreciate comments about yedoma studies from Jens Strauss.

515

References

Bjella, K. Dalton Highway 9 to 11 Mile Expedient Resistivity Permafrost Investigation, Alaska Department of Transportation and Public Facilities Technical Report, FHWA-AK-RD-13-08, Fairbanks, Alaska, 2014.

Bjella, K.: Imaging of Ground Ice with Surface Based Geophysics, ERDC/CRREL Technical Report TR-15-14, Hanover, NH. USA, 2015.

Bjella, K.: Improving Design Methodologies and Assessment Tools for Building on Permafrost in a Warming Climate, ERDC/CRREL Technical Report TR-20-13, Hanover, NH. USA, 2020.

Boike, J., Roth, K., and Overduin, P. P.: Thermal and hydrologic dynamics of the active layer at a continuous permafrost site (Taymyr Peninsula, Siberia), Water Resourc. Res., 34(3), 355-63, 1998.

Bray, M. T., French, H. M., and Shur, Y.: Further cryostratigraphic observations in the CRREL permafrost tunnel, Fox, Alaska, Permafrost Periglac. Process., 17(3), 233-243, 2006.

Brown, D. R. N., Jorgenson, M. T., Douglas, T. A., Romanovsky, V., Kielland, K., and Euskirchen, E.: Vulnerability of permafrost to fire-initiated thaw in lowland forests of the Tanana Flats, interior Alaska, J. Geophys. Res. Biogeosci., doi: 10.1002/2015JG003033, 2015.

Burkert A., Douglas T. A., Waldrop, M. P. , Mackelprang, R.: Changes in the active, dead, and dormant microbial community structure across a Pleistocene permafrost chronosequence, Appl. Environ. Microbio., 1, 85(7), 2019.

Chasmer, L. and Hopkinson, C.: Threshold loss of discontinuous permafrost and landscape evolution, Glob. Change Biol., 23, 2672-2686, doi:10.1111/gcb.13537, 2017.

Circumpolar Active Layer Monitoring Network, www2.gwu.edu/~calm/data/north.htm, 2020.

Douglas, T. A., Jorgenson, M. T., Kanevskiy, M. Z., Romanovsky, V. E., Shur, Y., and Yoshikawa, K.: Permafrost dynamics at the Fairbanks Permafrost Experimental Station near Fairbanks, Alaska, Proceedings of the Ninth International Conference on Permafrost, D. Kane, and K. Hinkel, eds. pp. 373, 2008.

Douglas, T. A., Fortier, D., Shur, Y. I., Kanevskiy, M. Z., Guo, L., Cai, Y., and Bray, M.: Biogeochemical and geocryological characteristics of wedge and thermokarst-cave ice in the CRREL Permafrost Tunnel, Alaska, Permafrost Periglac. Process., doi: 10.1002/ppp.709, 2011.

Douglas, T. A., Blum, J. D., Guo, L., Keller, K., and Gleason, J. D.: Hydrogeochemistry of seasonal flow regimes in the Chena River, a subarctic watershed draining discontinuous permafrost in interior Alaska (USA), Chem. Geol., 335, 48-62, 2013.

Douglas, T. A., Jones, M. C., Hiemstra, C. A., and Arnold, J.: Sources and sinks of carbon in boreal ecosystems of Interior Alaska: Current and future perspectives for land managers, Elementa: Sci. of the Anthropocene, 2, 2014.

Douglas, T. A., Jorgenson, M. T., Brown, D. R. N., Campbell, S. W., Hiemstra, C. A., Saari, S. P., Bjella, K., and Liljedahl, A. K.: Degrading permafrost mapped with electrical resistivity tomography, airborne imagery and LiDAR, and seasonal thaw measurements, Geophysics, 81, 1, doi: 10.1190/GEO2015-0149.1, 2016.

Douglas, T. A. and Mellon, M. T.: Sublimation of terrestrial permafrost and the implications for ice-loss processes on Mars, Nature Comm., 10, 1, 2019.

Douglas, T. A., Turetsky, M. R., and Koven, C. D.: Increased rainfall stimulates permafrost thaw across a variety of Alaskan ecosystems, npj Climate Atmos. Sci., 3, 1, 1-7. 2020.

Friedlingstein, P., Jones, M. W., O'sullivan, M., Andrew, R. M., Hauck, J., Peters, G. P., Peters, W., Pongratz, J., Sitch, S., Quéré, C. L., Bakker, D.C.: Global carbon budget 2019, Earth Sys. Sci. Data., 4, 11(4), 1783-838, 2019.

Grosse, G., Harden, J., Turetsky, M., McGuire, A. D., Camill, P., Tarnocai, C., Frolking, S., Schuur, E. A., Jorgenson, T., Marchenko, and S., Romanovsky, V.: Vulnerability of high-latitude soil organic carbon in North America to disturbance, J. Geophys. Res. Biogeosci., 116, G4, 2011.

Hamilton, T. D., Craig, J. L. and Sellmann, P. V. The Fox permafrost tunnel: A late Quaternary geologic record in central Alaska, Geol. Soc. Amer. Bull., 100, 6, 948–969, 1988.

Harada, K. and Yoshikawa, K.: Permafrost age and thickness near Adventfjorden, Spitsbergen, Polar Geography, 20, 4, 267-281, 1996.

Harada, K., Wada, K., and Fukuda, M.: Permafrost mapping by transient electromagnetic method, Permafrost Periglac. Process., 11, 71-84, 2000.

Heslop, J. K., Winkel, M., Walter Anthony, K. M., Spencer, R. G., Podgorski, D. C., Zito, P., Kholodov, A., Zhang, M., Liebner, S.: Increasing organic carbon biolability with depth in yedoma permafrost: ramifications for future climate change, J. Geophys. Res.: Biogeosci., 124(7), 2021-38, 2019.

Hinkel, K. M. and Nelson, F. E.: Spatial and temporal patterns of active layer thickness at Circumpolar Active Layer Monitoring (CALM) sites in northern Alaska, 1995–2000, J. Geophys. Res., 108,D2, 8168, doi:10.1029/2001JD000927, 2003.

Hjort, J., Karjalainen, O., Aalto, J. Westermann, S., Romanovsky, V. E., Nelson, F. E., Etzelmüller, B., Luoto, M.: Degrading permafrost puts Arctic infrastructure at risk by mid-century, Nat. Comm., 9, 5147, doi: 10.1038/s41467-018-07557-4, 2018.

Hoekstra, P.: Electromagnetic probing of permafrost. In: Proceedings of 2nd International Conference on Permafrost, Yakutsk, USSR, North American Contribution (pp. 517-526), National Academy of Science, 1973.

Hubbard, T. D., Braun, M. L., Westbrook, R. E., and Gallagher, P. E.: High-resolution lidar data for infrastructure corridors, Fairbanks Quadrangle, Alaska,, in: Hubbard, T.D., Koehler, R.D., and Combellick, R.A., High-resolution lidar data for Alaska infrastructure corridors, Alaska Division of Geological & Geophysical Surveys Raw Data File 2011-3E. doi: 10.14509/22727, 2011.

Hubbard, S. S., Gangodagamage, C., Dafflon, B., Wainwright, H., Peterson, J., Gusmeroli, A., Ulrich, C., Wu, Y., Wilson, C., Rowland, J., Tweedie, C., and Wullscheleger, S. D.: Quantifying and relating land-surface and subsurface variability in permafrost environments using LiDAR and surface geophysical datasets, Hydrogeol. J., 21, 1, 149-169, 2013.

Jafarov, E. E., Romanovsky, V. E, Genet, H., McGuire, A. D., Marchenko, S. S.: The effects of fire on the thermal stability of permafrost in lowland and upland black spruce forests of interior Alaska in a changing climate, Environ. Res. Lett., 8,3, 035030, 2013.

Johnstone, J. F., Chapin, F. S., Hollingsworth, T. N., Mack, M. C., Romanovsky, V., Turetsky, M.: Fire, climate change, and forest resilience in interior Alaska, Canadian J. For. Res., 40,7, 1302-12, 2010.

Jones, B. M., Stoker, J. M., Gibbs, A. E., Grosse, G., Romanovsky, V. E., Douglas, T. A., Kinsman, N. E. M., and Richmond, B. M.: Quantifying landscape change in an arctic coastal lowland using repeat airborne LiDAR, Environ. Res. Lett., 8, 045025, doi:10.1088/1748-9326/8/4/045025, 2013.

Jorgenson, M. T., Racine, C. H., Walters, J. C., Osterkamp, T. E.: Permafrost degradation and ecological changes associated with a warming climate in central Alaska, Clim. Change, 48(4), 551-79, 2001.

Jorgenson, M. and Osterkamp, T.: Response of boreal ecosystems to varying modes of permafrost degradation, Can. J. For. Res., 35, 9, 2100–2111, 2005.

Jorgenson, M. T., Yoshikawa, K., Kanevskiy, M., Shur, Y., Romanovsky V, Marchenko S, Grosse G, Brown J, Jones B.: Permafrost characteristics of Alaska, Proceedings of the Ninth International Conference on Permafrost, edited by D. Kane, and K. Hinkel, Vol. 29, p. 121-122, 2008.

Jorgenson, M. T., Harden, J., Kanevskiy, M., O'Donnell, J., Wickland, K., Ewing, S., Manies, K., Zhuang, Q., Shur, Y., Striegl, R., Koch, J.: Reorganization of vegetation, hydrology and soil carbon after permafrost degradation across heterogeneous boreal landscapes, Environ. Res. Lett., 16, 8(3):035017, 2013.

Jorgensen, T., Meidlinger, D.: The Alaska Yukon Region of the Circumboreal Vegetation map (CBVM), Conservation of Arctic Flora and Fauna (CAFF). 2015.

Jorgenson, M. T., Douglas, T. A., Liljedahl, A. K., Roth, J. E., Cater, T. C., Davis, W. A., Frost, G. V., Miller, P. F., and Racine, C. H. The roles of climate extremes, ecological succession, and hydrology in cycles of permafrost aggradation and degradation in fens on the Tanana Flats, Alaska, J. Geophys. Res. Biogeosci. doi: 10.1029/2020JG005824, 2020.

Kanevskiy, M., Shur, Y., Fortier, D., Jorgenson, M. T., Stephani, E.: Cryostratigraphy of late Pleistocene syngenetic permafrost (yedoma) in northern Alaska, Itkillik River exposure, Quat. Res., 75(3), 584-96, 2011

Kasischke, E. S. and Johnstone, J. F.: Variation in postfire organic layer thickness in a black spruce forest complex in interior Alaska and its effects on soil temperature and moisture, Can. J. For. Res., 35, 9, 2164-77, 2005.

Kneisel, C.: Assessment of subsurface lithology in mountain environments using 2D resistivity imaging, Geomorphol., 80,1, 32-44, 2006.

Kokelj, S. V. and Jorgenson, M. T.: Advances in Thermokarst Research, Permafrost Periglac. Process., 24, 108-119, 2013.

Kropp, H., and 48 others Vegetation stature controls air-soil temperature coupling across pan-Arctic ecosystems, Environ. Res. Lett. Doi: 10.1088/1748-9326/abc994, 2020.

Lader, R., Walsh, J. E., Bhatt, U. S., and Bieniek, P. A.: Projections of twenty-first-century climate extremes for Alaska via dynamical downscaling and quantile mapping, Journal of Appl. Meteorol. Climatol., 56, 9, 2393-409, 2017.

Latifovic, R., Pouliot, D., and Olthof, I., Circa 2010 Land Cover of Canada: Local Optimization Methodology and Product Development, Rem. Sens., 9(11), 1098; http://www.mdpi.com/2072-4292/9/11/1098, 2017

Lewkowicz, A. G., Etzelmüller, B., and Smith, S.L.: Characteristics of discontinuous permafrost based on ground temperature measurements and electrical resistivity tomography, southern Yukon, Canada, Permafrost Periglac. Process., 22, 4, 320-342, 2011.

Lewkowicz, A. G., Way, R. G.: Extremes of summer climate trigger thousands of thermokarst landslides in a High Arctic environment, Nature Comm., 10, 1, 2019.

Liljedahl, A. K., Boike, J., Daanen, R. P., Fedorov, A. N., Frost, G. V., Grosse, G., Hinzman, L. D., Iijma, Y., Jorgenson, J. C., Matveyeva, N., Necsoiu, M.: Pan-Arctic ice-wedge degradation in warming permafrost and its influence on tundra hydrology, Nature Geosci., 4, 312-8, 2016.

Liston, G. E., Hiemstra, C.A.: The changing cryosphere: Pan-Arctic snow trends (1979–2009). J. Climate, 1;24(21), 5691-712, 2011.

Loke, M. H., Barker, R. D.: Rapid least-squares inversion of apparent resistivity pseudosections by a quasi-Newton method 1, Geophys. Prospect., 44(1), 131-52, 1996.

Loke, M. H., Acworth, I., and Dahlin, T.: A comparison of smooth and blocky inversion methods in 2D electrical imaging surveys, Exploration Geophys., 34, 182-187, 2003.

Loranty, M. M. and 18 others: Changing ecosystem influences on soil thermal regimes in northern high-latitude permafrost regions. Biogeosci., doi: 10.5194/bg-15-5287-2018, 2018

Mackelprang, R., Waldrop, M. P., DeAngelis, K. M., David, M. M., Chavarria, K. L., Blazewicz, S. J., Rubin, E. M., and Jansoon, J. K.: Metagenomic analysis of a permafrost microbial community reveals a rapid response to thaw, Nature, 480, 368-371, 2011.

Mackelprang, R., Burkert, A., Haw, M., Mahendrarajah, T., Conaway, C. H., Douglas, T. A., Waldrop, M. P.: Microbial survival strategies in ancient permafrost: insights from metagenomics, The ISME Journal, 11(10), 2305-18, 2017.

McClymont, A. F., Hayashi, M., Bentley, L. R., Christensen, B.S.: Geophysical imaging and thermal modeling of subsurface morphology and thaw evolution of discontinuous permafrost, J. Geophys. Res.: Earth Surface, 118(3), 1826-37, 2013.

Messan, K. S., Jones, R. M., Doherty, S. J., Foley, K., Douglas, T. A., and Barbato, R.A.: The role of changing temperature in microbial metabolic processes during permafrost thaw, PloS one, 15, 4, p.e0232169, 2020.

Minsley, B., Wellman, T. P., Walvoord, M. A., Revil, A.: Sensitivity of airborne geophysical data to sublacustrine and near-surface permafrost thaw, The Cryosphere 9(2), 781-94, 2015.

Minsley, B. J., Pastick, N. J., Wylie, B. K., Brown, D. R., Kass, M. A.: Evidence for nonuniform permafrost degradation after fire in boreal landscapes, J. Geophys. Res. Earth Surf., 121, 2, 320-35, 2016.

Myers-Smith, I., Harden, J., Wilmking, M., Fuller, C., McGuire, A, and Chapin, F. S.: Wetland succession in a permafrost collapse: interactions between fire and thermokarst, Biogeosc., 5, 5, 2008.

Neumann, R. B., Moorberg, C. J., Lundquist, J. D., Turner, J. C., Waldrop, M. P., McFarland, J. W., Euskirchen, E. S., Edgar, C. W., and Turetsky, M. R.: Warming effects of spring rainfall increase methane emissions from thawing permafrost, Geophysi. Res. Lett., 46, 3, 1393-401, 2019.

Nicholas, J. R. and Hinkel, K. M.: Concurrent permafrost aggradation and degradation induced by forest clearing, central Alaska, USA, Arctic, Ant., Alp. Res., 28, 1996.

Nossov, D. R., Jorgenson, M. T., Kielland, K., Kanevskiy, M. Z.: Edaphic and microclimatic controls over permafrost response to fire in interior Alaska, Environ. Res. Lett. 8(3), 035013, 2013.

Osterkamp, T. and Romanovsky, V.: Evidence for warming and thawing of discontinuous permafrost in Alaska, Permafrost Periglac. Process., 10, 1, 17–37, 1999.

Pastick, N., J., Jorgenson, M. T., Wylie, B. K., Nield, S. J., Johnson, K. D., Finley, A. O.: Distribution of near-surface permafrost in Alaska: Estimates of present and future conditions, Rem. Sens. Environ., 168, 301-15, 2015.

Phillips, M. R., Burn, C. R., Wolfe, S. A., Morse, P. D., Gaanderse, A. J., O'Neill, H. B., Shugar, D. H., and Gruber, S.: Improving water content description of ice-rich permafrost soils, Proceedings GeoQuébec, 2015;68, 2015.

Racine, C. H. and Walters, J. C.: Groundwater-discharge fens in the Tanana Lowlands, Interior Alaska, U.S.A., Arctic Alpine Res., 26, 4, 418-426, 1994.

Raynolds, M. K, Walker, D. A., Balser, A., Bay, C., Campbell, M., Cherosov, M. M., Daniëls, F. J., Eidesen, P. B., Ermokhina, K. A., Frost, G. V., Jedrzejek, B.: A raster version of the Circumpolar Arctic Vegetation Map (CAVM), Rem. Sens. Environ., 232, 111297, 2019.

Rey, D. M., Walvoord, M. A., Minsley, B. J., Ebel, B. A., Voss, C. I., and Singha, K.: Wildfire initiated talik development exceeds current thaw projections: Observations and models from Alaska's continuous permafrost zone, Geophys. Rese. Lett., e2020GL087565, 2020.

Schuster, P. F., Schaefer, K. M., Aiken, G. R., Antweiler, R. C., Dewild, J. F., Gryziec, J. D., Gusmeroli, A., Hugelius, G., Jafarov, E., Krabbenhoft, D. P., Liu, L.: Permafrost stores a globally significant amount of mercury, Geophys. Res. Lett., 45(3), 1463-71, 2018.

Shiklomanov, N. I., Streletskiy, D. A., Nelson, F. E., Hollister, R. D., Romanovsky, V. E., Tweedie, C. E., Bockheim, J. G., and Brown, J.: Decadal variations of active-layer thickness in moisture-controlled landscapes, Barrow Alaska, J. Geophys. Res., 115, G00I04, doi:10.1029/2009JG001248, 2010.

Shur, Y. L., Hinkel, K. M., and Nelson, F. E.: The transient layer: Implications for geocryology and global-change science, Permafrost Periglac. Process., 16, 5–17, 2005.

Shur, Y. and Jorgenson, M.: Patterns of permafrost formation and degradation in relation to climate and ecosystems, Permafrost Periglac. Process., 18, 1, 7–19, 2007.

Smith, L. C., Sheng, Y., MacDonald, G. M., Hinzman, L. D.: Disappearing Arctic lakes, Science, 308, 5727, 1429-1429, 2005.

Strauss, J., Schirrmeister, L., Grosse, G., Wetterich, S., Ulrich, M., Herzschuh, U., Hubberten, H. W.: The deep permafrost carbon pool of the Yedoma region in Siberia and Alaska, Geophys. Res. Lett., 40(23), 6165-70, 2013.

Strauss, J., Laboor, S., Fedorov, A. N.: Database of ice-rich Yedoma permafrost (IRYP), PANGAEA, https://doi.org/10.1594/PANGAEA.861733, 2016.

Strauss, J., Schirrmeister, L., Grosse, G., Fortier, D., Hugelius, G., Knoblauch, C., Romanovsky, V., Schädel, C., von Deimling, T. S., Schuur, E. A., Shmelev, D.: Deep Yedoma permafrost: A synthesis of depositional characteristics and carbon vulnerability, Earth Sci. Rev., 172, 75-86, 2017.

Vonk, J. E., Mann, P. J., Dowdy, K. L., Davydova, A., Davydov, S. P., Zimov, N., Spencer, R. G,, Bulygina, E. B., Eglinton, T. I., Holmes, R. M.: Dissolved organic carbon loss from Yedoma permafrost amplified by ice wedge thaw, Environ. Res. Lett., 8(3), 035023, 2013.

Walker, M. D., Wahren, C. H., Hollister, R. D., Henry, G. H., Ahlquist, L. E., Alatalo, J. M., Bret-Harte, M. S., Calef, M. P., Callaghan, T. V., Carroll, A. B., Epstein, H. E.: Plant community responses to experimental warming across the tundra biome. Proc. . U.S. Nat. Acad. Sci., 103. 1342-1346, 2006.

Way, R. G., Lewkowicz, A. G., Zhang, Y.: Characteristics and fate of isolated permafrost patches in coastal Labrador, Canada, The Cryosphere, 12(8), 2667-88, 2018.

Wendler, G. and Shulski, M.: A century of climate change for Fairbanks, Alaska, Arctic, 62, 295–300, 2009.

Wilhelm, R. C., Niederberger, T. D., Greer, C., and Whyte, L. G.: Microbial diversity of active layer and permafrost in an acidic wetland from the Canadian High Arctic, Can., J., Microbiol., 57, 303-315, 2011.

Wolken, J. M., Hollingsworth, T. N., Rupp, T. S., Chapin, III, F. S., Trainor, S. F., Barrett, T. M., Sullivan, P. F., McGuire, A. D., Euskirchen, E. S., Hennon, P. E., and Beever, E. A..: Evidence and implications of recent and projected climate change in Alaska's forest ecosystems, Ecosphere, 2, 11, 1-35, 2011.

Yi, Y., Kimball, J. S., Chen, R., Moghaddam, M., Reichle, R. H., Mishra, U., Zona, D., and Oechel, W. C.: Characterizing permafrost active layer dynamics and sensitivity to landscape spatial heterogeneity in Alaska, The Cryosphere, 12, 1, 145, 2018.

Yoshikawa, K., Hinzman, L. D.: Shrinking thermokarst ponds and groundwater dynamics in discontinuous permafrost near Council, Alaska, Permafrost Periglac. Proc., (2), 151-60, 2003.

Yoshikawa, K., Leuschen, C., Ikeda, A., Harada, K., Gogineni, P., Hoekstra, P., Hinzman, L., Sawada, Y., and Matsuoka, N.: Comparison of geophysical investigations for detection of massive ground ice (pingo ice), J. Geophys. Res.: Planets (1991–2012), 111 E6, 2006.

Table 1. A summary of the thaw depth measurements by ecotype and results from a means comparison using a student's t-test. Among a given ecotype different and year the letters identify statistically significantly different means. Mean values for a given ecotype and year with similar letters have similar means.

	Year	N	Mean (cm)	Standard deviation	Means comparison	% increase 2013-2020
Tussock	2013	126	45.0	10.9	F	
	2014	153	67.7	12.2	D	50
	2015	153	63.3	12.6	E	41
	2016	153	75.3	12.1	A	67
	2017	153	72.2	13.8	B, C	60
	2018	153	69.5	13.3	C, D	54
	2019	153	72.8	13.9	A, B	62
	2020	153	73.5	13.4	A, B	63
Wetland	2013	41	71.5	24.4	D	
	2014	48	91.4	23.5	B, C	28
	2015	48	82.7	18.6	C, D	16
	2016	48	104.9	30.0	A, B	47
	2017	46	96.9	30.4	B, C	36
	2018	47	103.1	39.2	A, B	44
	2019	47	113.3	49.4	A	59
	2020	47	113.6	51.5	A	59
Disturbed	2013	35	75.5	23.8	C	
	2014	67	85.8	20.4	C	14
	2015	58	84.2	21.1	C	11
	2016	60	99.9	28.8	B	32
	2017	51	101.9	33.0	B	35
	2018	56	104.3	35.0	B	38
	2019	55	118.4	42.4	A	57
	2020	56	117.1	44.3	A	55

Table 1. Continued

	Year	N	Mean (cm)	Standard deviation	Means comparison	% increase 2013-2020
Mixed forest	2013	57	64.4	17.9	D	
	2014	75	81.4	19.0	B, C	27
	2015	75	75.1	17.2	C	17
	2016	75	85.1	27.1	B	32
	2017	75	79.5	24.0	B, C	24
	2018	74	84.9	25.7	B	32
	2019	74	93.4	29.0	A	45
	2020	74	97.4	30.2	A	51
Moss spruce	2013	86	54.6	13.3	E	
	2014	111	59.7	10.7	C, D	9
	2015	120	56.5	12.6	D, E	3
	2016	118	64.0	11.6	B	17
	2017	124	62.5	12.2	B, C	14
	2018	115	64.9	14.8	B	19
	2019	119	70.1	16.0	A	28
	2020	115	72.5	18.7	A	33

730

Table 2. A summary of thermistor measurements from 1.2m depth at the study site transects. Mean annual temperature (MAT) values for each of six individual years are presented as well as the six year global mean annual temperature for each site.

Creamer's Field, disturbed		MAT °C	Creamer's Field, 1m-polygon center		MAT °C	Creamer's Field, 1m- ice wedge in mixed forest		MAT °C
10/01/13	09/30/14	2.78	10/01/13	09/30/14	-0.36	10/01/13	09/30/14	-0.37
10/01/14	09/30/15	4.57	10/01/14	09/30/15	-0.29	10/01/14	09/30/15	-0.33
10/01/15	09/30/16	3.85	10/01/15	09/30/16	-0.26	10/01/15	09/30/16	-0.23
10/01/16	09/30/17	4.91	10/01/16	09/30/17	-0.23	10/01/16	09/30/17	-0.20
10/01/17	09/30/18	5.15	10/01/17	09/30/18	-0.16	10/01/17	09/30/18	-0.10
10/01/18	09/30/19	4.61	10/01/18	09/30/19	-0.13	10/01/18	09/30/19	-0.08
10/01/19	09/30/20	N/A	10/01/19	09/30/20	-0.11	10/01/19	09/30/20	-0.06
	6 year mean	4.31		7 year mean	-0.22		7 year mean	-0.20
Creamer's Field- mixed forest		MAT °C	Creamer's Field- tussocks		MAT °C	Farmer's Loop 1- mixed forest		MAT °C
10/01/13	09/30/14	-0.72	10/01/13	09/30/14	-2.85	10/01/13	09/30/14	-0.21
10/01/14	09/30/15	-0.20	10/01/14	09/30/15	-3.03	10/01/14	09/30/15	-0.08
10/01/15	09/30/16	-0.23	10/01/15	09/30/16	-1.63	10/01/15	09/30/16	-0.07
10/01/16	09/30/17	-0.15	10/01/16	09/30/17	-0.34	10/01/16	09/30/17	-0.04
10/01/17	09/30/18	-0.13	10/01/17	09/30/18	-0.51	10/01/17	09/30/18	-0.02
10/01/18	09/30/19	-0.12	10/01/18	09/30/19	-1.31	10/01/18	09/30/19	0.00
10/01/19	09/30/20	-0.11	10/01/19	09/30/20	-1.15	10/01/19	09/30/20	0.06
	7 year mean	-0.24		7 year mean	-1.55		7 year mean	-0.05
Farmer's Loop 2, 240m-tussocks		MAT °C	Farmer's Loop 2, 245m-tussocks		MAT °C	Permafrost Tunnel- spruce forest		MAT °C
10/01/13	09/30/14	-2.29	10/01/13	09/30/14	-3.70	10/01/13	09/30/14	-0.74
10/01/14	09/30/15	-2.62	10/01/14	09/30/15	-3.20	10/01/14	09/30/15	-1.17
10/01/15	09/30/16	-0.68	10/01/15	09/30/16	-2.16	10/01/15	09/30/16	-0.40
10/01/16	09/30/17	-1.45	10/01/16	09/30/17	-2.98	10/01/16	09/30/17	-0.98
10/01/17	09/30/18	-0.63	10/01/17	09/30/18	-1.80	10/01/17	09/30/18	-0.28
10/01/18	09/30/19	-0.55	10/01/18	09/30/19	-2.21	10/01/18	09/30/19	-0.27
10/01/19	09/30/20	-1.51	10/01/19	09/30/20	-2.16	10/01/19	09/30/20	-0.25
	7 year mean	-1.39		6 year mean	-2.60		7 year mean	-0.58

735

Figure 1. A Worldview 2 (© Digital Globe) satellite image of the area around Fairbanks, Alaska (red dot on inset map) identifying the field site sites (colored regions) and transects (white lines) in this study.

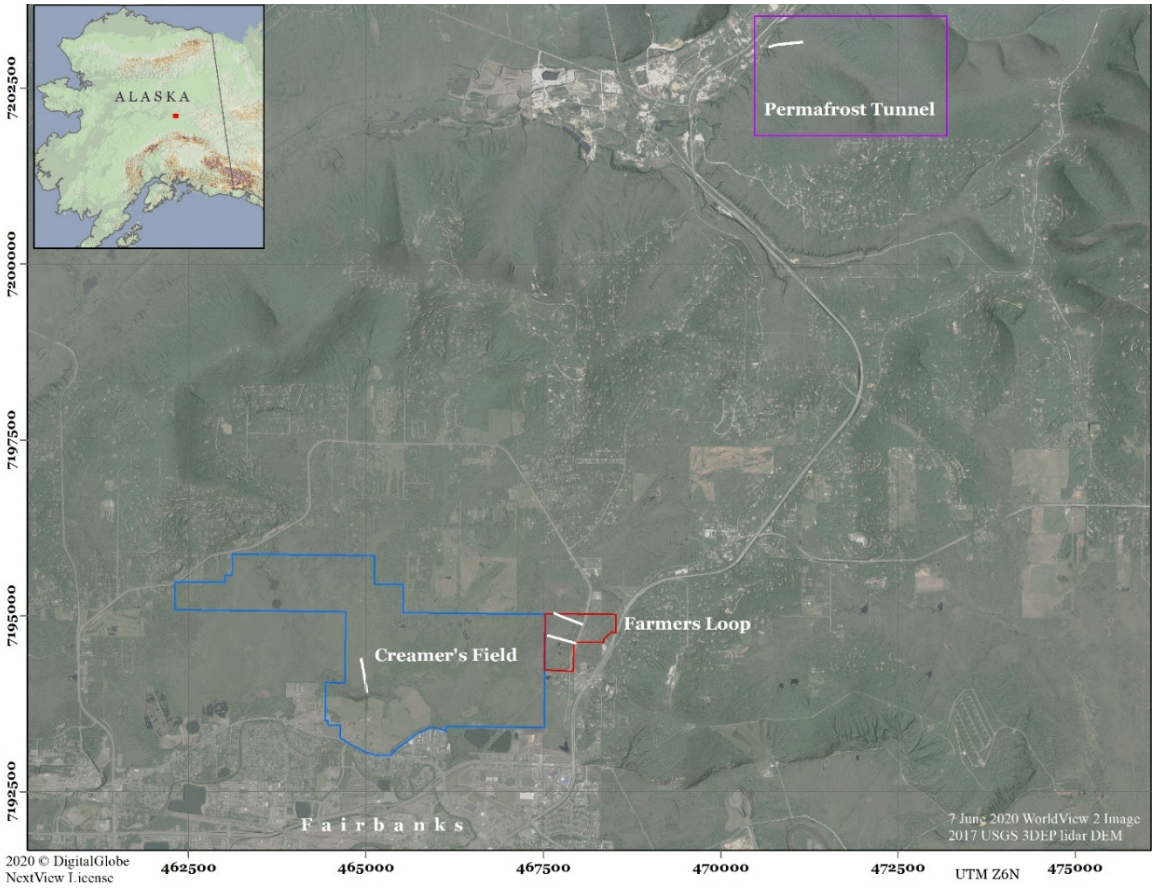

740

Figure 2. The Creamer's Field transect from 0 to 246 m (white line in Fig. 1). Image a) is a Worldview 2 (© Digital Globe) true color image of the transect (white line) with terrain features and core locations (circles) identified, b) LiDAR, c) repeat thaw depth measurements in 2014, d) repeat active layer depth measurements from 2014-2019, and e) a 246 m electrical resistivity tomography transect corrected for ground surface elevation with boreholes identified as black boxes to true depth and numbers corresponding to the distance (in meters) of the borehole location along the transect. Stars with a "T" denote a thermistor location.

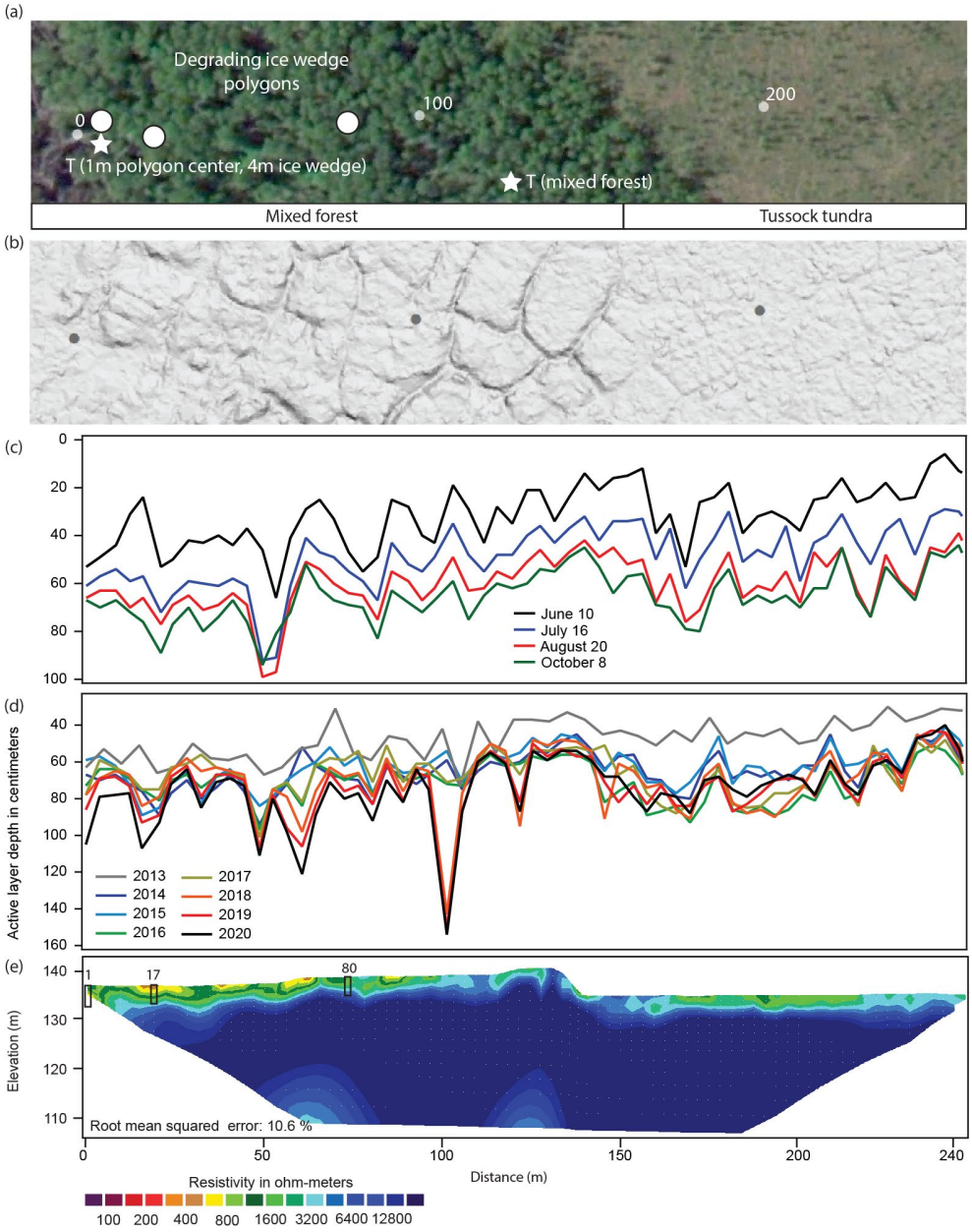

Figure 3. The Creamer's Field transect from 252 to 498 m (white line in Fig. 1). Image a) is a Worldview 2 (© Digital Globe) true color image of the transect (white line) with terrain features and core locations (circles) identified, b) May 2020 LiDAR, c) repeat thaw depth measurements in 2014, d) repeat active layer depth measurements from 2014-2019, and e) is a 246 m electrical resistivity tomography transect corrected for ground surface elevation with boreholes identified as black boxes to true depth and numbers corresponding to the distance (in m) of the borehole location along the transect. Stars with a "T" denote a thermistor location.

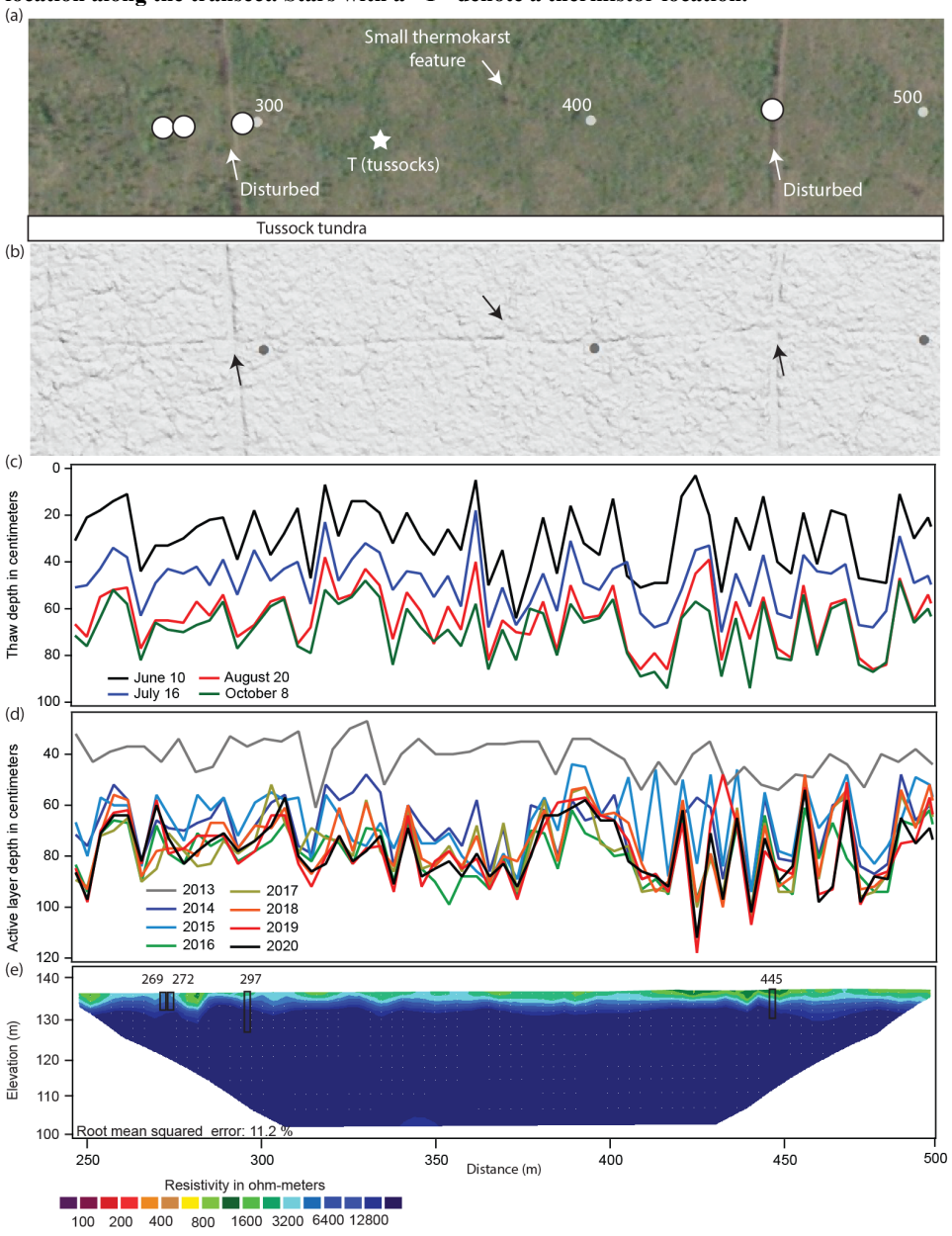

Figure 4. The Farmer's Loop 1 transect (white line in Fig. 1). Image a) is a Worldview 2 (© Digital Globe) true color image of the transect (white line) with terrain features and core locations (circles) identified, b) May 2020 LiDAR, c) repeat thaw depth measurements in 2014, d) repeat active layer depth measurements from 2014-2019, and e) a 410 m electrical resistivity tomography transect corrected for ground surface elevation with boreholes identified as black boxes to true depth and numbers corresponding to the distance (in m) of the borehole location along the transect. Stars with a "T" denote a thermistor location.

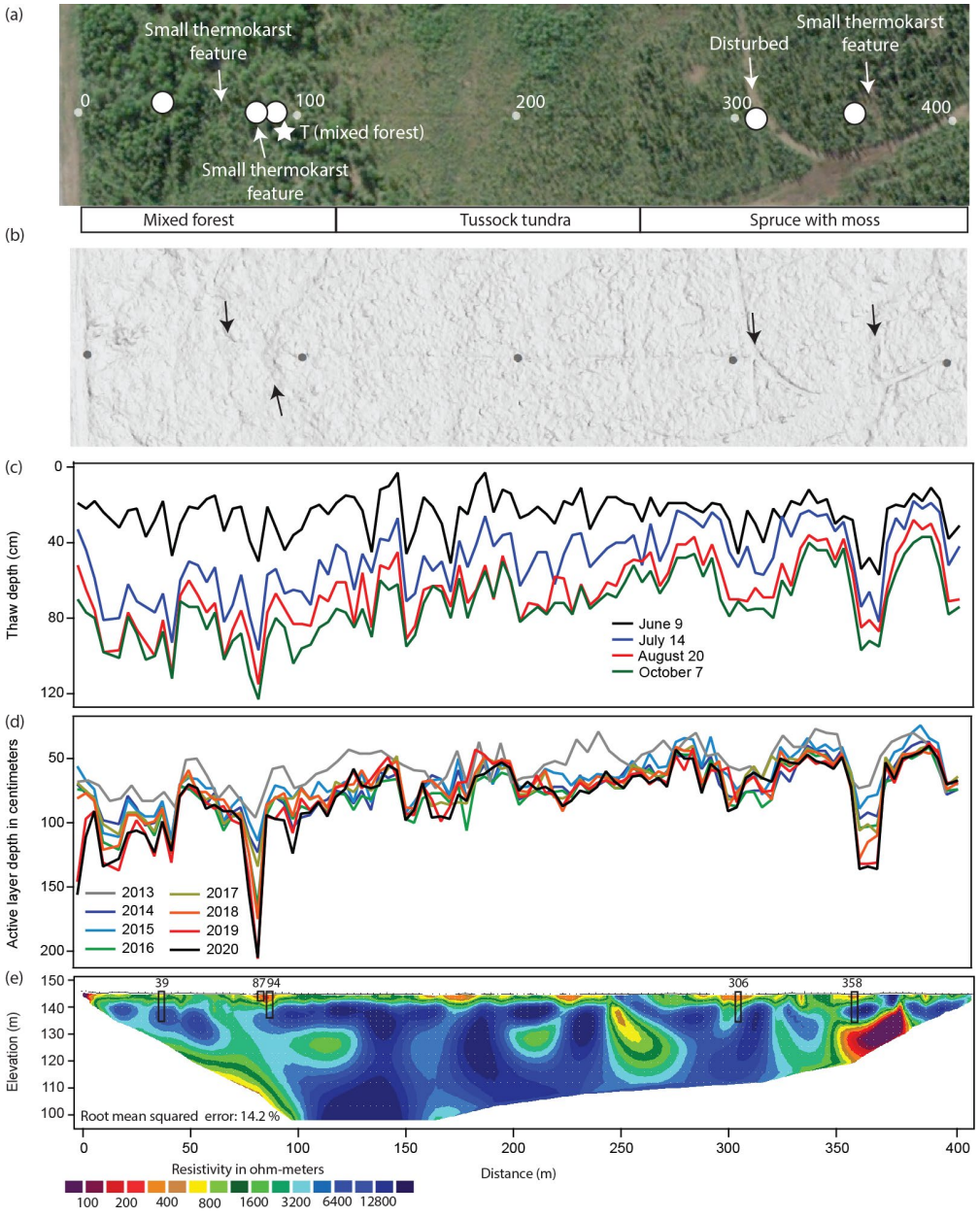

Figure 5. The Farmer's Loop 2 transect (white line in Fig. 1). Image a) is a Worldview 2 (© Digital Globe) true color image of the transect (white line) with terrain features and core locations (circles) identified, b) May 2020 LiDAR, c) repeat thaw depth measurements in 2014, d) repeat active layer depth measurements from 2014-2019, and e) a 492 m electrical resistivity tomography transect corrected for ground surface elevation with boreholes identified as black boxes to true depth and numbers corresponding to the distance (in m) of the borehole location along the transect. Stars with a "T" denote a thermistor location.

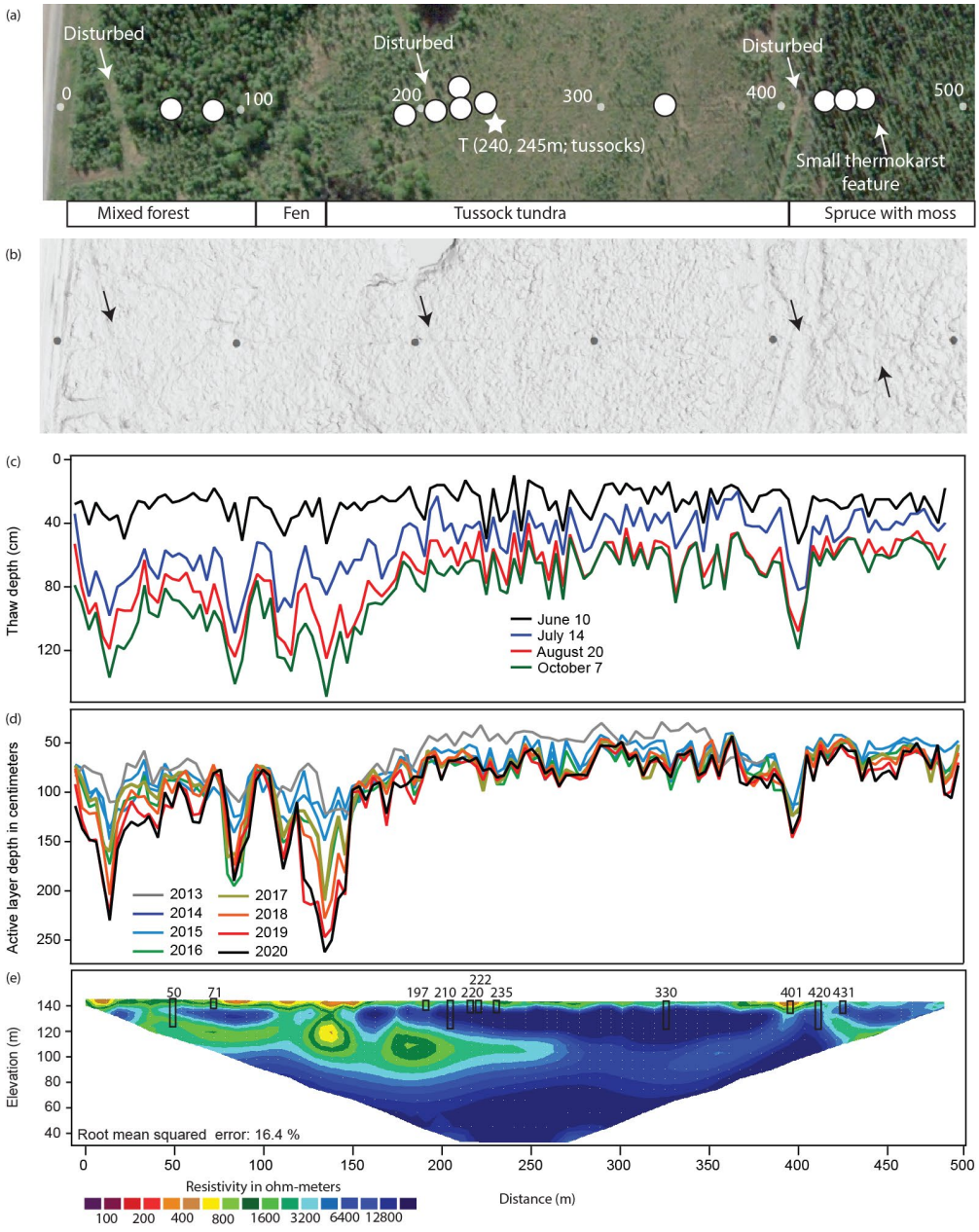

Figure 6. The Permafrost Tunnel transect (white line in Fig. 1). Image a) is a Worldview 2 (© Digital Globe) true color image of the transect (white line) with terrain features and core locations (circles) identified, b) May 2020 LiDAR, c) repeat thaw depth measurements in 2014, d) repeat active layer depth measurements from 2014-2019, and e) a 410 m electrical resistivity tomography transect corrected for ground surface elevation with boreholes identified as black boxes to true depth and numbers corresponding to the distance (in m) of the borehole location along the transect. Stars with a "T" denote a thermistor location.

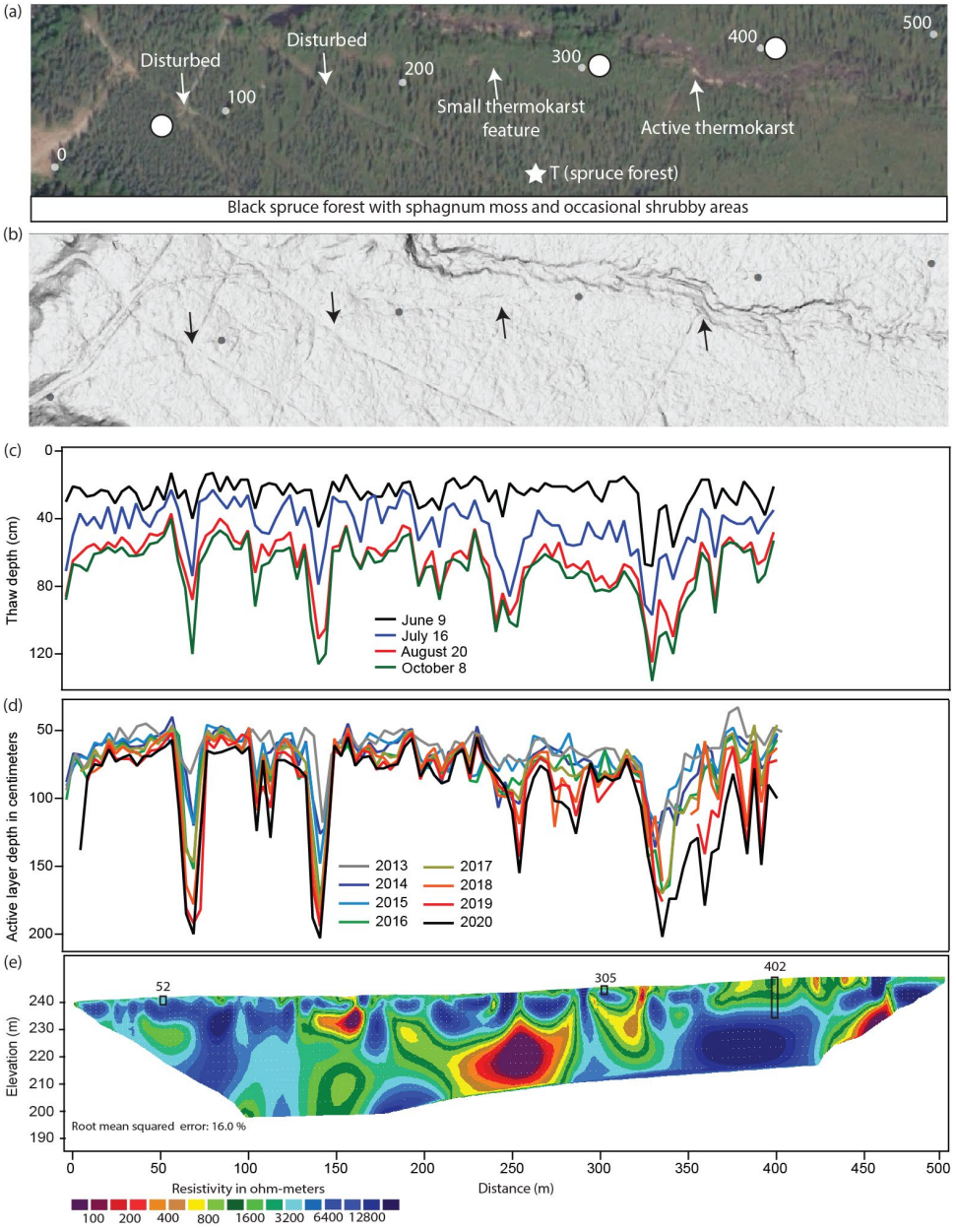

Figure 7. Figure 7. Past (2010) elevations were subtracted from current (2020) elevations at the Creamer's Field site (2020 minus 2010). The 500 m transect is denoted by the white line. Negative values identify regions of thaw degradation and subsidence over the ten year period. Positive values show elevation gains due to deeper water and vegetation.

780

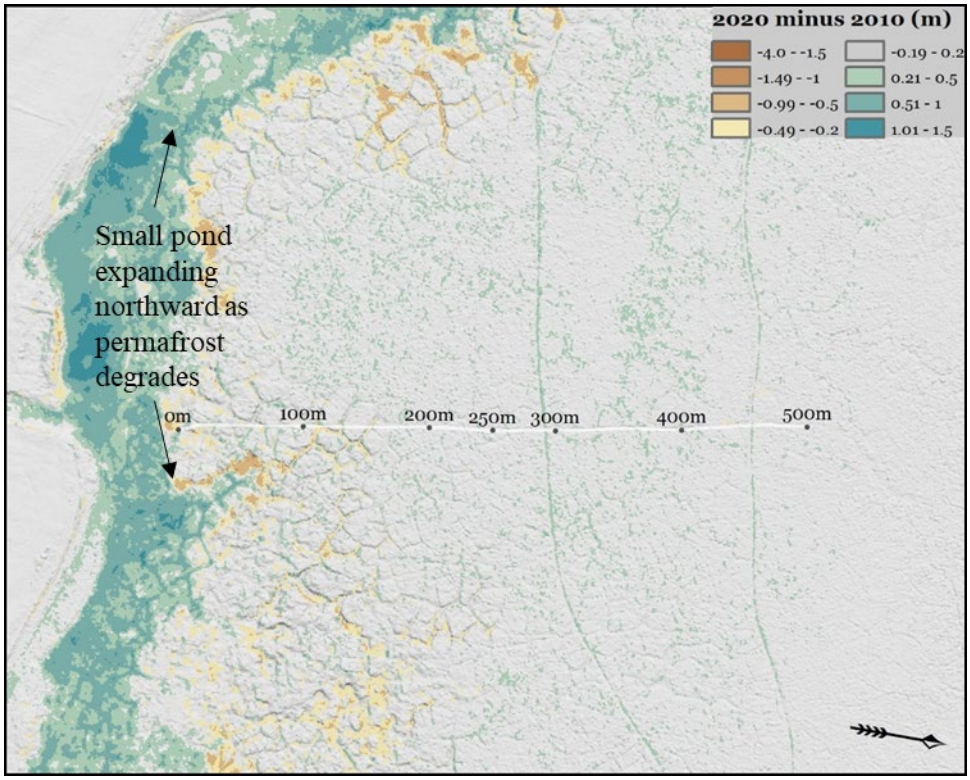

Figure 8. Meteorologic conditions from April 1, 2013 through October 31, 2014. Top: air temperature from the Permafrost Tunnel and Farmer's Loop sites and historical daily mean values between 1929 and 2019 at the National Weather Service's Fairbanks International Airport (PAFA) site. Middle and bottom: precipitation at the PAFA site.

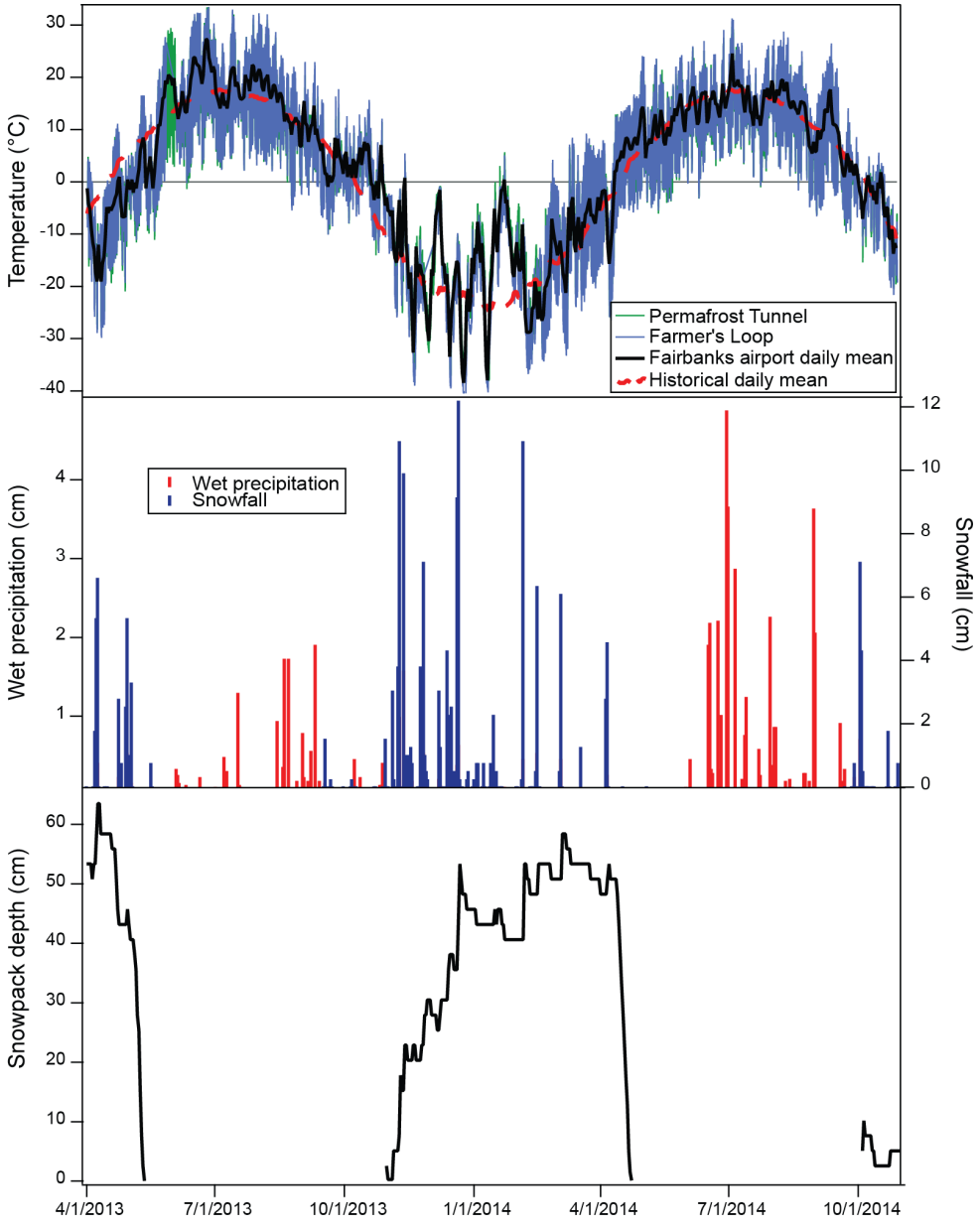

Figure 9. Soil temperature measurements at 1.2 m depth from October 1, 2013 to October 1, 2019 for the three study sites. Mean annual ground temperature (MAGT) values at 1.2 m for the period of record are also provided.

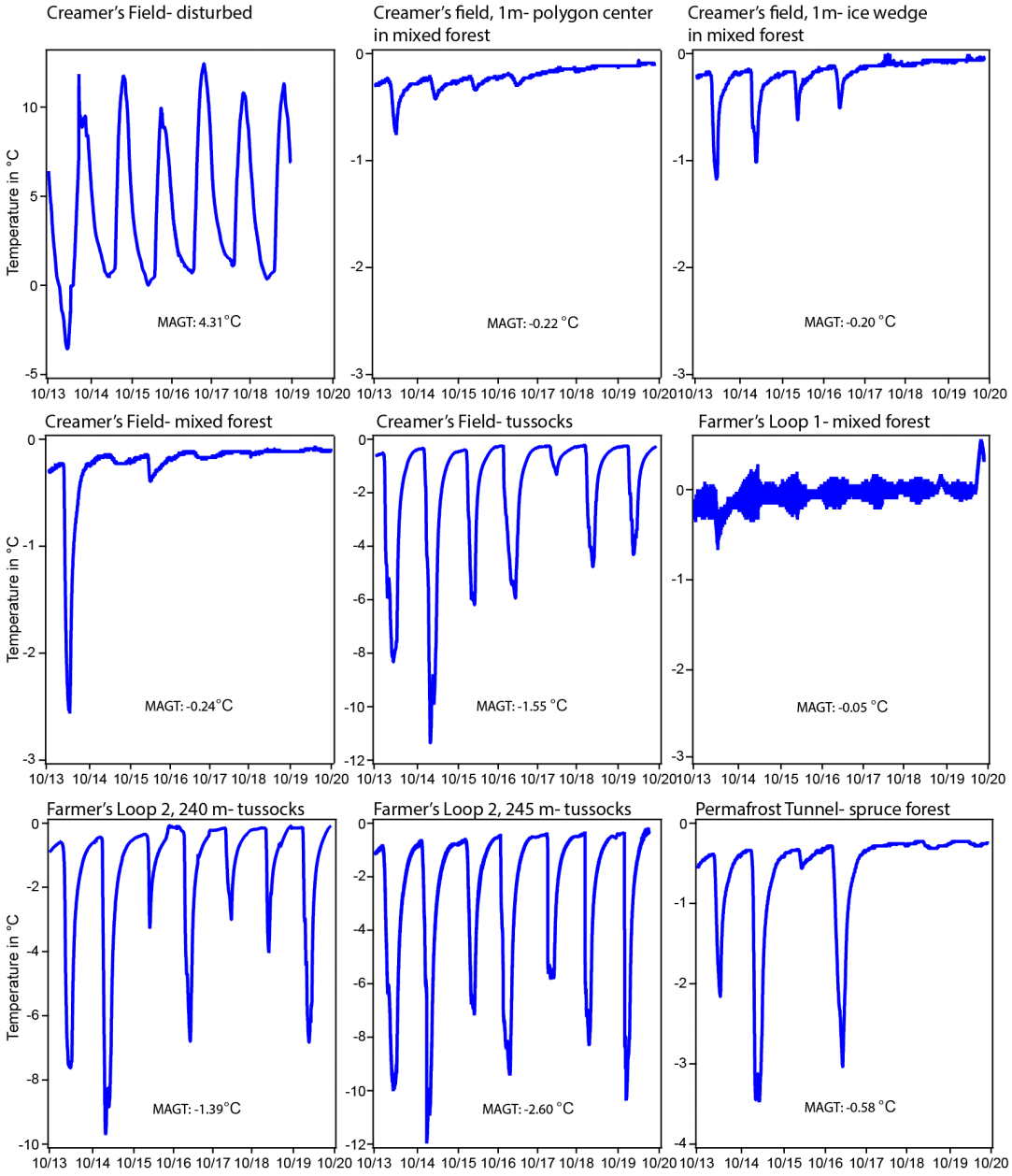

Figure 10. A) a ~~© Google Earth~~ map identifying yedoma type permafrost (yellow) in Alaska (Strauss et al., 2016) and locations of six central Alaska Circumpolar Active Layer Monitoring sites with records of at least 15 years. The focused field sites in this study are all near Farmer's Loop. The white bounding box represents the 500,000 km^2 area of central Alaska across which the study measurements are extrapolated. B) active layer measurements from the six CALM sites from Interior Alaska and the Seward Peninsula. Data from CALM (2020).

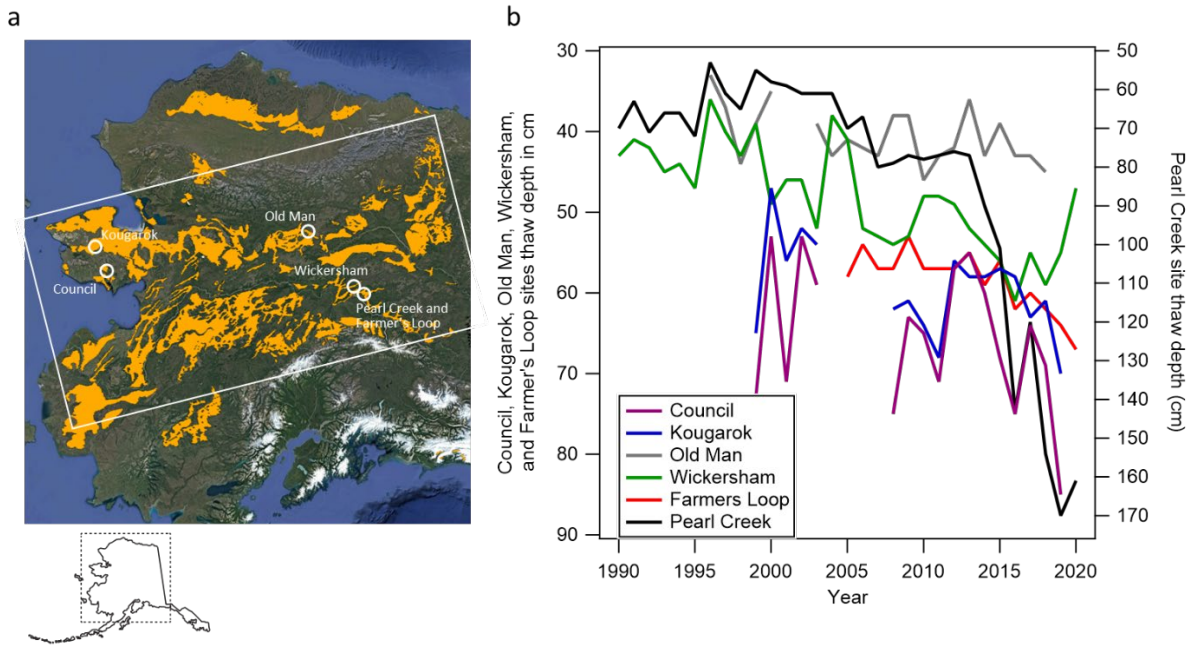

Table S1. A summary of the cores collected during this study.

Creamer's Field transect

64.8677N, 147.7383W

Distance: 1 m	Depth start (cm)	Depth finish (cm)	Gravimetric moisture content (g/g) %	Description
2/25/2014	75	90	743.1	Organics with ice
Geoprobe	120	135	223.4	Organics with ice
	180	195	376.5	Organics with ice
	240	255	40.7	Silt with no visible ice
	270	285	38.5	Sandy silt with no visible ice
	300	315	32.1	Sandy silt with no visible ice
	345	360	37.5	Silt with no visible ice
	390	405	25	Silty sand
	435	450	28.9	Silty sand
	510	525	29.5	Silty sand

64.8679N, 147.7384W

Distance: 17 m	Depth start (cm)	Depth finish (cm)	Gravimetric moisture content (g/g) %	Description
2/25/2014	45	60	281.7	Thawed; Organics with ice
Geoprobe	60	255	N/A	Ice wedge ice
	270	285	54.3	Silty sand
	300	315	30.8	Silty sand
	375	390	26.2	Sand
	435	450	27.8	Sand

64.8683N, 147.7389W

Distance: 80 m	Depth start (cm)	Depth finish (cm)	Gravimetric moisture content (g/g) %	Frozen bulk density (kg/m^3)	Description
5/2/2017	0	15	85.8	1079	Peat
SIPRE	15	30	80.3	1113	Peat
	30	54	71.3	973	Peat
	54	71	81.0	1155	Peat
	71	92	72.6	946	Peat
	92	106	79.6	1046	Peat
	106	127	81.8	1012	Peat
	127	145	93.3	1095	Peat
	145	161	79.6	1017	Peat
	161	178	86.4	1040	Peat with minor ice visible
	178	196	84.6	1039	Peat with minor ice visible
	196	220	79.3	1034	Peat with minor ice visible
	220	234	77.3	1140	Peat with minor ice visible
	234	249	79.8	1117	Peat with minor ice visible
	249	268	68.4	1090	Silt with minor ice visible
	268	297	32.1	776	Silt with minor ice visible
	297	317	63.2	1043	Silty sand
	317	337	51.1	1297	Sand
	337	351	71.0	1389	Sand
	351	368	49.4	1240	Sand

64.8701N, 147.7393W

Distance: 269 m	Depth start (cm)	Depth finish (cm)	Gravimetric moisture content (g/g) %	Frozen bulk density (kg/m^3)	Description
5/3/2017	0	8	71.7	754	Peat with visible ice
SIPRE	8	21	95.2	1045	Peat with visible ice
	21	35	86.6	1083	Peat with visible ice
	35	49	78.4	1269	Peat with visible ice
	49	63	81.1	1202	Peat with visible ice
	63	75	93.7	1096	Peat with visible ice
	75	80	254.1	3159	Peat with visible ice
	80	96	80.1	895	Peat with visible ice
	96	110	81.9	904	Peat with visible ice
	110	127	87.1	925	Peat with visible ice
	127	144	83.7	912	Silt with minor ice visible
	144	159	86.5	958	Silt with minor ice visible
	159	173	81.9	943	Silt with minor ice visible
	173	185	95.5	1100	Silt with minor ice visible
	185	197	88.8	1009	Silt with minor ice visible
	197	213	95.9	1090	Silt with minor ice visible
	213	230	92.9	1051	Silt with minor ice visible
	230	255	71.4	865	Silt with minor ice visible
	255	273	86.3	1058	Silt with minor ice visible
	273	289	86.4	1200	Silt with minor ice visible
	289	306	87.8	1230	Silt with minor ice visible
	306	322	86.9	1231	Silt with minor ice visible
	322	332	89.3	1109	Silt with minor ice visible
	332	342	92.6	1221	Silt with minor ice visible

64.8701N, 147.7393W

Distance: 272 m	Depth start (cm)	Depth finish (cm)	Gravimetric moisture content (g/g) %	Description
2/27/2014	30	45	446	Peat with visible ice
Geoprobe	90	105	519.7	Peat with visible ice
	135	150	488.5	Peat with visible ice
	195	210	486.4	Peat with visible ice
	285	300	130.6	Silt with visible ice
	345	360	210.8	Silt with visible ice

64.8703N, 147.7394W

Distance: 297 m	Depth start (cm)	Depth finish (cm)	Gravimetric moisture content (g/g) %	Description
3/4/2014	105	120	579.4	Organics with visible ice
Geoprobe	225	240	1230	Organics with visible ice
	285	300	37.1	Silt with organics and visible ice
	324	339	112.8	Silt with visible ice
	369	384	112.2	Silt with visible ice
	390	405	86.55	Silt with visible ice
	405	420	107.9	Silt with no visible ice
	426	441	93.1	Silt with no visible ice
	444	459	53.1	Silt with no visible ice
	480	495	36.8	Sandy silt
	510	525	36	Sandy silt
	540	555	43.1	Sandy silt
	600	615	42.1	Silt with no visible ice
	645	660	36.4	Silt with no visible ice
	720	735	51.4	Silt with no visible ice
	750	765	33.5	Sand
	810	825	44.6	Silty sand with organics
	855	870	32.6	Sand
	930	945	33.9	Sandy silt with gravel

64.8716N, 147.7400W

Distance: 445 m	Depth start (cm)	Depth finish (cm)	Gravimetric moisture content (g/g) %	Description
2/27/2014	21	36	307.1	Organics with visible ice
Geoprobe	90	105	244	Organics with visible ice
	150	165	101.6	Silt with visible ice
	180	195	98.7	Silt with no visible ice
	204	219	139.6	Silt with no visible ice
	225	240	52.4	Silt with no visible ice
	279	294	179	Silt with organics and no visible ice
	294	309	84.8	Silt with visible ice
	315	330	114.1	Silt with organics and visible ice
	360	465	91.4	Silt with minor visible ice
	390	405	182	Silt with no visible ice
	414	429	131.1	Silt with minor visible ice
	450	465	107.5	Silt with no visible ice
	510	525	94.4	Silt with no visible ice
	570	585	94.3	Silt with no visible ice
	615	630	182.9	Silt with no visible ice
	660	675	219.7	Silt with no visible ice
	690	705	36.7	Sandy silt with no visible ice

Farmer's Loop transect 1

64.8767, 147.6751 W

Distance: 39 m	Depth start (cm)	Depth finish (cm)	Gravimetric moisture content (g/g) %	Description
3/25/2014	75	90	29.2	Silt with no visible ice
Geoprobe	90	105	82.7	Peaty silt
	120	135	44.4	Peaty silt with visible ice
	165	180	22.7	Silt with no visible ice
	225	240	48.4	Silt with no visible ice
	279	294	115.7	Silt with visible ice
	312	327	45.3	Silt with no visible ice
	327	342	123.4	Silt with minor peat
	360	375	46.2	Silt with no visible ice
	420	435	98	Silt with no visible ice
	450	465	98.9	Silt with minor peat
	480	495	95.1	Silt with no visible ice
	510	525	65	Silt with no visible ice
	570	585	77.2	Silt with no visible ice
	591	606	256.2	Peat
	645	660	41.3	Silt with no visible ice
	675	690	49.8	Silt with no visible ice
	705	720	36.9	Silt with no visible ice
	765	780	34.1	Silt with no visible ice
	840	855	94.6	Silt with no visible ice
	930	945	32.3	Silt with no visible ice
	1050	1065	38.5	Silt with no visible ice
	1110	1125	37.6	Silt with no visible ice
	1170	1185	36.1	Silt with no visible ice
	1215	1230	34.5	Silt with no visible ice
	1260	1275	47.2	Silt with no visible ice
	1335	1350	38.1	Silt with no visible ice

64.8765N, 147.6766W

Distance: 87 m	Depth start (cm)	Depth finish (cm)	Gravimetric moisture content (g/g) %	Frozen bulk density (kg/m^3)	Description
5/3/2017	0	16	88.2	1032	Peat
SIPRE	16	32	56.3	1364	Silt with peat
	32	46	76.6	1176	Silt with peat
	46	62	79.1	1360	Thawed silty peat
	62	73	63.0	1038	Thawed silty peat
	73	84	59.5	1133	Thawed silty peat
	84	102			Missing; thawed silty mud
	102	116	87.5	1267	Silt with minor ice visible
	116	128	75.0	1647	Silt with minor ice visible
	128	136	98.4	2104	Silt with minor ice visible
	136	149	57.9	1653	Silt with minor ice visible
	149	160	88.5	1519	Silt with minor ice visible
	160	171	84.3	1523	Silt with minor ice visible
	171	182	83.2	1548	Silt with minor ice visible
	182	191	74.7	1424	Silt with minor ice visible

64.8769N, 147.6763W

Distance: 94 m	Depth start (cm)	Depth finish (cm)	Gravimetric moisture content (g/g) %	Description
4/22/2014	90	105	59.9	Silt with no visible ice
Geoprobe	114	129	201.9	Peat
	135	150	68.6	Silt with no visible ice
	180	195	77.6	Silt with no visible ice
	210	225	111.8	Peaty silt with visible ice
	225	240	66.8	Silt with minor visible ice
	255	270	31.6	Silt with no visible ice
	300	315	83.3	Peaty silt with visible ice
	375	390	95.3	Peaty silt with visible ice
	390	405	111.3	Peaty silt with visible ice
	420	435	87.4	Silt with no visible ice
	465	480	54.5	Silt with no visible ice
	495	510	40.4	Silt with no visible ice
	510	525	75.9	Silt with minor visible ice
	540	555	34.1	Silt with no visible ice
	585	600	46.7	Silt with minor visible ice
	615	630	104.2	Silt with minor visible ice
	645	660	46.4	Peaty silt with visible ice
	690	705	46.7	Silt with no visible ice
	735	750	37.2	Silt with minor visible ice
	750	765	33.2	Silt with minor visible ice
	810	825	99.4	Peaty silt with visible ice
	825	840	79.7	Silt with minor visible ice
	855	870	34.2	Silt with minor visible ice
	870	885	42.8	Silt with minor visible ice
	960	975	35.6	Silt with minor visible ice

64.8776N, 147.6804W

Distance: 306 m	Depth start (cm)	Depth finish (cm)	Gravimetric moisture content (g/g) %	Description
4/2/2014	60	75	341	Organics with visible ice
Geoprobe	105	120	514.1	Organics with visible ice
	195	210	355.6	Organics with visible ice
	420	435	52.3	Silt with minor visible ice
	456	471	37.6	Silt with minor visible ice
	480	495	82.5	Silt with no visible ice
	540	555	117	Organic rich silt
	570	585	78	Silt with minor visible ice
	600	615	59.6	Silt with minor visible ice
	615	630	40.6	Silt with minor visible ice
	660	675	330.9	Peat with visible ice
	705	720	338.5	Peat with visible ice
	780	795	43.4	Silt with minor visible ice
	840	855	39.6	Silt with minor visible ice
	900	915	40.1	Silt with minor visible ice
	945	960	47.7	Silt with minor visible ice
	1020	1022		Wood fragment ^{14}C age: 10,360 +/- 260; $\delta^{13}C$: -27.7 per mil; Lab Sample name: GX-33790; Field sample name: FLT1306-34-34.5
	1050	1065	64.4	Silt with minor visible ice
	1080	1095	41.8	Silt with minor visible ice
	1155	1170	79.9	Silt with minor visible ice
	1230	1245	35	Silt with minor visible ice
	1275	1290	30.8	Silt with minor visible ice
	1290	1305	39.6	Silt with minor visible ice
	1365	1380	20.6	Silt with minor visible ice

64.8778N, 147.6814W

Distance: 358 m	Depth start (cm)	Depth finish (cm)	Gravimetric moisture content (g/g) %	Description
3/26/2014	120	135	324.4	Organics with visible ice
Geoprobe	225	240	187.8	Silt with organics
	360	375	54.9	Silt
	420	435	45	Silt with minor ice
	450	465	41	Silt
	471	486	216.7	Peat layer
	480	495	95.1	Silt
	525	540	781.2	Peat with visible ice
	645	660	62.6	Peat with visible ice
	667	669		Wood fragment ^{14}C age: 10,160 +/- 160; $\delta^{13}C$: -28.0 per mil; Lab sample name: GX-33790; Field sample name: FLT1358#8-21-21.5
	750	765	234	Peat with minor visible ice
	834	849	301.4	Silt with visible ice
	915	930	161.2	Soft thawed silt
	1020	1035	213.1	Soft thawed silt

Farmer's Loop transect 2

64.8744N, 147.6774W

Distance: 50 m	Start (cm)	End (cm)	Gravimetric moisture content (g/g) %	Description
5/5/2014	30	45	26.6	Organics
Geoprobe	90	105	48.5	Silt with no visible ice
	120	135	34.7	Silt with no visible ice
	150	165	50.8	Silt with no visible ice
	195	210	42.0	Silt with no visible ice
	315	330	52.4	Silt with no visible ice
	360	375	71.4	Silt with no visible ice
	435	450	95.6	Silt with minor visible ice
	540	555	40.5	Silt with no visible ice
	585	600	29.9	Silt with no visible ice
	675	690	31.9	Silt with no visible ice
	735	750	35.9	Silt with no visible ice
	780	795	36.5	Silt with no visible ice
	825	840	38.4	Silt with no visible ice
	870	885	43.9	Silt with no visible ice
	900	915	43.2	Silt with no visible ice
	960	975	55.0	Silt with minor visible ice

64.8745N, 147.6779W

Distance: 71 m	Start (cm)	End (cm)	Description
5/25/2018	0	15	Organics
SIPRE	15	60	Sandy silt with no visible ice
	60	84	Silt with peat
	84	117	Thawed silty peat
	117	165	Silt with visible ice
	174	222	Silt with visible ice
	222	345	Silt with visible ice

64.8746N, 147.6806W

Distance: 197 m	Start (cm)	End (cm)	Gravimetric moisture content (g/g) %	Frozen bulk density (kg/m^3)	Description
5/3/2017	0	22	43.8	950	Organics
SIPRE	22	36	73.1	1515	Silt with visible ice
	36	48	33.8	1607	Silt with visible ice
	48	61	51.4	1708	Silt with visible ice
	61	76	52.3	1494	Silt with visible ice
	76	90	46.0	1537	Silt with visible ice
	90	106	148.3	1294	Silt with visible ice
	106	123	66.7	1287	Peat with visible ice
	123	132	301.7	1326	Peat with visible ice
	132	145	138.6	1370	Peat with visible ice
	145	159	100.8	1356	Peat with visible ice
	159	174	88.3	1406	Silt with visible ice
	174	187	52.5	1538	Silt with visible ice
	187	201	55.0	1402	Silt with visible ice

64.8747N, 147.6809W

Distance: 210 m	Start (cm)	End (cm)	Gravimetric moisture content (g/g) %	Description
5/1/2014	90	105	185.2	Organics with peat
Geoprobe	120	135	122.4	Silt with visible ice
	165	180	202.2	Peat with visible ice
	225	240	199.6	Silt with visible ice
	270	285	153	Silt with visible ice
	315	330	79.0	Silt with no visible ice
	375	390	56.44	Silt with visible ice
	390	405	56.8	Silt with visible ice
	435	450	69.7	Silt with visible ice
	525	540	49.7	Silt with minor visible ice
	570	585	44.8	Silt with minor visible ice
	645	660	37.9	Silt with no visible ice
	690	705	41.9	Silt with no visible ice
	780	795	42.5	Silt with no visible ice
	825	840	44.7	Silt with no visible ice
	900	915	44.3	Silt with no visible ice
	945	960	46.1	Silt with no visible ice
	1020	1035	48.4	Silt with no visible ice
	1065	1080	48.1	Silt with visible ice

64.8748N, 147.6813W

Distance: 220 m	Start (cm)	End (cm)	Description
5/25/2018	0	15	Organics with peat
SIPRE	15	27	Peat with minor silt layers
	30	66	Peat
	66	81	Peat with minor silt layers
	81	120	Peat with minor silt layers
	120	138	Peat with minor silt layers
	138	153	Silt with visible ice
	153	264	Ice with silt
	264	318	Ice with silt

64.8749N, 147.6814W

Distance: 222 m	0	15	Organics with peat
5/25/2018	15	111	Peat with minor silt layers
SIPRE	111	150	Peat with minor silt layers and visible ice
	150	219	Silt with visible ice
	219	267	Silt with visible ice

64.8748N, 147.6815W

Distance: 235 m	Start (cm)	End (cm)	Gravimetric moisture content (g/g) %	Frozen bulk density (kg/m^3)	Description
5/3/2017	0	13	82.3	935	Organics with peat
SIPRE	13	26	91.1	1221	Organics with peat
	26	40	92.8	1158	Organics with peat
	40	54	72.7	1004	Organics with peat
	54	68	79.1	940	Organics with peat
	68	82	88.8	1206	Organics with peat
	82	90	74.4	1018	Organics with peat
	90	104	77.4	1088	Organics with peat
	104	119	52.5	1109	Silt with visible ice
	119	129	78.0	781	Clear ice
	129	138	78.3	1080	Peat with visible ice
	138	150	88.5	1038	Peat with visible ice
	150	163	82.6	1186	Peat with visible ice
	163	173	85.1	1193	Peat with visible ice
	173	192	69.9	992	Peat with visible ice
	192	210	73.4	1080	Silt with visible ice
	210	234	48.8	1058	Silt with visible ice
	234	256	62.9	1065	Silt with visible ice

64.8750N, 147.6833W

Distance: 330 m	Start (cm)	End (cm)	Gravimetric moisture content (g/g) %	Description
5/2/2014	45	60	544.6	Organics with peat
Geoprobe	90	105	648.4	Silt with visible ice
	150	165	648.4	Silt with visible ice
	240	255	117.4	Silt with visible ice
	255	270	144.1	Silt with visible ice
	345	360	69.0	Silt with visible ice
	375	390	253.7	Silt with visible ice
	405	420	419.1	Silt with visible ice
	435	450	234.6	Silt with organics and visible ice
	465	480	341.4	Silt with organics and visible ice
	495	510	561.7	Silt with organics and visible ice
	510	5250	774.8	Silt with organics and visible ice
	555	570	517.9	Silt with organics and visible ice
	600	615	128.0	Silt with visible ice
	630	645	397.1	Silt with organics and visible ice
	675	690	387.6	Silt with organics and visible ice
	705	720	321.6	Silt with organics and visible ice
	735	750	114.2	Silt with organics and visible ice
	795	810	63.7	Silt with organics and visible ice
	840	855	63.6	Silt with visible ice
	870	885	65.0	Silt with visible ice
	975	990	89.7	Organic rich silt with visible ice
	1020	1035	79.5	Silt with minor visible ice
	1080	1095	47.6	Silt with minor visible ice

64.8753N, 147.6846W

Distance: 401 m	Start (cm)	End (cm)	Gravimetric moisture content (g/g) %	Frozen bulk density (kg/m^3)	Description
5/3/2017	0	15	87.3	1150	Organics with peat
SIPRE	15	27	98.7	1136	Organics with peat
	27	37	91.4	1241	Organics with peat
	37	53	35.6	1572	Silt with visible ice
	53	69	32.6	1616	Silt with visible ice
	69	83	28.8	1697	Silt with visible ice
	83	100	62.0	1450	Silt with visible ice
	100	114	46.7	1361	Silt with visible ice
	114	128	84.4	1373	Silt with visible ice
	128	142	60.9	1594	Silt with visible ice
	142	156	76.9	1490	Silt with visible ice
	156	176	37.7	1233	Silt with visible ice
	176	197	50.2	1323	Silt with visible ice

64.8752N, 147.6851W

Distance: 420 m	Start (cm)	End (cm)	Gravimetric moisture content (g/g) %	Description
5/8/2014	90	105	69.6	Silt with no visible ice
Geoprobe	150	165	31.3	Silt with no visible ice
	240	255	88.9	Silt with no visible ice
	300	315	44.4	Silt with visible ice
	360	375	55.7	Silt with visible ice
	390	405	76.2	Silt with visible ice
	435	450	518.0	Ice rich peat
	493	495		Peat sample ^{14}C age: 7,200 +/- 190; $d^{13}C$: -28.7 per mil; Lab sample name: GX-33789; Field sample name: FLT2420-15-5-16.5
	540	555	85.2	Silt with visible ice
	600	615	57.2	Silt with visible ice
	690	705	41.5	Silt with visible ice
	750	765	44.1	Silt with minor visible ice
	810	825	43.0	Silt with minor visible ice
	930	945	39.6	Silt with minor visible ice
	1020	1035	40.8	Silt with no visible ice

64.8753N, 147.6854W

Distance: 431 m	Start (cm)	End (cm)	Gravimetric moisture content (g/g) %	Frozen bulk density (kg/m^3)	Description
5/3/2017	0	6	69.4	815	Organics with peat
SIPRE	6	21	88.6	1145	Organics with peat
	21	34	78.4	1143	Organics with peat
	34	45	105.6	1436	Organics with peat
	45	59	65.0	1180	Organics with peat
	59	72	93.4	1188	Silt with visible ice
	72	84	91.7	1338	Silt with visible ice
	84	106	55.8	1097	Silt with no visible ice
	106	118	70.0	1591	Silt with no visible ice
	118	132	59.4	1394	Silt with no visible ice
	132	147	50.6	1494	Silt with no visible ice
	147	161	55.6	1565	Silt with no visible ice
	161	175	58.9	1617	Silt with no visible ice
	175	188	63.6	1500	Silt with no visible ice
	188	200	81.9	1482	Silt with no visible ice
	200	220	40.6	1078	Silt with no visible ice

Permafrost Tunnel Transect

64.9507N, 147.6196W

Distance: 52 m	Depth start (cm)	Depth finish (cm)	Description
6/5/2018	0	17	Thawed peat
SIPRE	17	31	Frozen silt with visible ice
	31	49	Muddy thawed silt
	49	74	Silt with visible ice
	74	100	Silt with visible ice

64.9510N, 147.6141W

Distance: 305 m	Depth start (cm)	Depth finish (cm)	Description
3/25/2018	0	15	Peat
SIPRE	15	45	Frozen silt with visible ice
	45	70	Muddy thawed silt
	70	249	Silt with visible ice

64.9511N, 147.6122W

Distance: 402 m	Depth start (cm)	Depth finish (cm)	Gravimetric moisture content (g/g) %	Description
3/5/2014	75	90	91.4	Silt with no visible ice
Geoprobe	150	165	148.8	Silt with no visible ice
	216	232.5	119.7	Silt with visible ice
	240	255	145.9	Silt with visible ice
	345	360	96.5	Silt with visible ice
	420	435	23.6	Silty sand
	495	510	77.7	Silt with visible ice
	585	600	57.5	Silt with visible ice
	645	660	83.3	Silt with visible ice
	720	735	57.2	Silt with visible ice
	930	945	53.4	Silt with visible ice
	1020	1035	85.9	Silt with visible ice
	1125	1140	94.1	Silt with visible ice
	1230	1245	66.8	Silt with visible ice
	1380	1395	56.3	Silt with visible ice
	1485	1500	37.3	Silt with visible ice
	1515	1530	25.3	Silt with visible ice
	1545	1560	40.7	Silt with visible ice